UNIVERSITY OF CALIFORNIA,
IRVINE

Fabrication of Nanoscale Spin Torque Oscillator Based on Pt/YIG

THESIS

submitted in partial satisfaction of the requirements
for the degree of

MASTER OF SCIENCE

in Physics

by

Christopher Safranski

Thesis Committee:
Professor Ilya Krivorotov, Chair
Professor Zuzanna Siwy
Professor Sasha Chernyshev

2018

TABLE OF CONTENTS

LIST OF FIGURES

ACKNOWLEDGMENTS

First off I would like to thank my advisor Ilya Krivorotov for the chance to work under him for these years. Not only has he been incredibly supportive, but patient as well when there are large gaps in knowledge. Also I would like to thank him for his monumental efforts to ensure that everyone in the lab was funded and was able to get the tools needed to further our research. I would also like to acknowledge the helpful group he has help put together which without, it would have been impossible to learn so much in these past years. Whether it be learning the first few things about the lab with Dr. Alejandro Jara, nanofab from Dr. Andrew Smith and Dr. Liu Yang, or Dr. Igor Barsukov handling the first round of questions all the time. I would like to also thank Dr. Yu-Jin Chen, Jen-Ru Chen, Han Kyu Lee, Chengcen Sha, Dr. Brian Youngblood,Dr. Jieyi Zhang for all the conversations about research and the sharing of knowledge.

ABSTRACT OF THE THESIS

Fabrication of Nanoscale Spin Torque Oscillator Based on Pt/YIG

By

Christopher Safranski

Master of Science in Physics

University of California, Irvine, 2018

Professor Ilya Krivorotov, Chair

Manipulation of magnetic materials by the spin degree of freedom is leading way to a new generation of electronics known as spintronics. The nanodevices using these properties are becoming attractive candidates for technological applications, since they can potentially consume less power than their semiconductor counterparts. One particular device of interest is the spin toque oscillator, which is a nanoscale source of microwave power. In this study, a spin torque oscillator based on the insulating material Yttrium Iron Garnet (YIG) is produced to study the effects of pure spin currents. In the process of reaching this goal, several types of preliminary developments are chronicled and new measurement techniques developed. The process of fabricating the YIG based nanodevices is described as well.

Chapter 1

Introduction

The manipulation of the spin degree of freedom has an important role in the development of novel electronic nanodevices. By moving away from electronics based on electron charge carriers, the hope is to significantly reduce the power needed to operate devices. With the ever increasing amount of nanodevices inside modern electronics, even a slight reduction in needed power per nanodevice will translate to a large amount of energy savings.

In this thesis, the background ideas behind spintronics and some groundwork done in preparation for research in the field will be presented. Chapter 1 will provide information on the basics of spintronics along with the concepts of magnetization dynamics. Chapter 2 will focus on the fabrication of a cryogenic measurement station and related tools for research. The next chapter will contain information on fabrication as well, but rather on the nanoscale and chronicle the fabrication of nanowires meant for spin torque oscillator studies. Lastly, Chapter 4 will cover some measurement techniques and example measurements on magnetic tunnel junctions and the nanowires fabricated in Chapter 3.

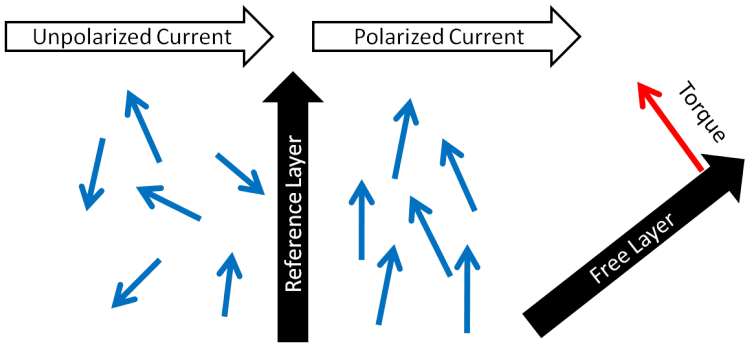

Figure 1.1: Toy model of the concept of spin torque, where charge current gets polarized by a field and then can exert a torque on a magnet.

1.1 Background

When speaking of the electronic devices designed in the past several decades, the most common theme is the movement of charge current mediated by electrons. This approach only takes into account the inherent charge of the electron and overlooks another important characteristic, its spin. An electron has a quantized unit of angular momentum and simply put, can be thought of as a charged bar magnet. In traditional electronics, this property is overlooked since the spins in simple materials are randomly distributed, resulting in zero net moment. Recently, experiments in spin polarizing charge current has given rise to the field of spintronics.

To understand how the spin degree of freedom can be manipulated and used to build a device, we will first consider a toy model. In this model shown in Figure 1.1, say we pass an electron gas through a region (Reference Layer) with a strong magnetic field. The electron's moment, as indicated by the blue arrows, will be aligned with the field from the region it passed through. If this polarized current is then passed into another moment (free layer), then they will exert a torque on it. The interaction of spin current on a magnetic moment is called spin torque [1]. Experimentally, application of large spin currents to a free magnetic layer have been shown to induce switching in multiple experiments [2–5].

While the observation of magnetic switching is important for technical applications, just considering this binary experiment ignores a rich amount of physics. In order to understand other phenomena, the basic principles of magnetization dynamics need to be understood. First, lets consider a magnetic moment sitting in a magnetic field. At equilibrium, the magnetic moment will align with the magnetic field. If it where then pulled out of equilibrium and released, it would then begin to oscillate around its equilibrium position conceptually much like a mass on a spring. However, unlike the simple nature of the restoring force for a mass on a spring, the magnetization obeys what is known as the Landau-Lifshitz-Gilbert (LLG) equation[6, 7]:

$$\frac{\partial \mathbf{M}}{\partial t} = -\gamma \left[\mathbf{M} \times \mathbf{H}_{\text{eff}}\right] + \frac{\alpha}{M_{\text{s}}} \left[\mathbf{M} \times \frac{\partial \mathbf{M}}{\partial t}\right], \tag{1.1}$$

Rather that oscillating back and forth like a mass on a spring, a more accurate mechanical analog of the resulting motion is a spinning top. A spinning top will precess about its angular momentum vector as it begins to fall over and much like this, the magnetization ($\mathbf{M}$) precesses about an effective field (H)as illustrated in Figure 1.2. The LLG equation contains two important parts. First is the field torque which is analogous to the stiffness of a spring for a harmonic oscillator and provides a restoring force. The second term describes the damping present in the system parameterized by the Gilbert damping coefficient α.

The addition of a spin torque from a spin current polarized in a direction $\mathbf{P}$ then modifies the LLG equation with the addition of two terms [1] resulting in:

$$\frac{\partial \mathbf{M}}{\partial t} = -\gamma \left[\mathbf{M} \times \mathbf{H}_{\text{eff}}\right] + \frac{\alpha}{M_{\text{s}}} \left[\mathbf{M} \times \frac{\partial \mathbf{M}}{\partial t}\right] - \frac{\gamma a}{M_{\text{s}}} \mathbf{M} \times \left[\mathbf{M} \times \mathbf{P}\right] - \gamma b \mathbf{M} \times \mathbf{P}, \tag{1.2}$$

They are often referred to as damping-like and field-like torques since their form acts as modifications to the original two terms of the LLG. The damping-like term strength is controlled by the parameter a, where the damping like term b and describe the magnitude of

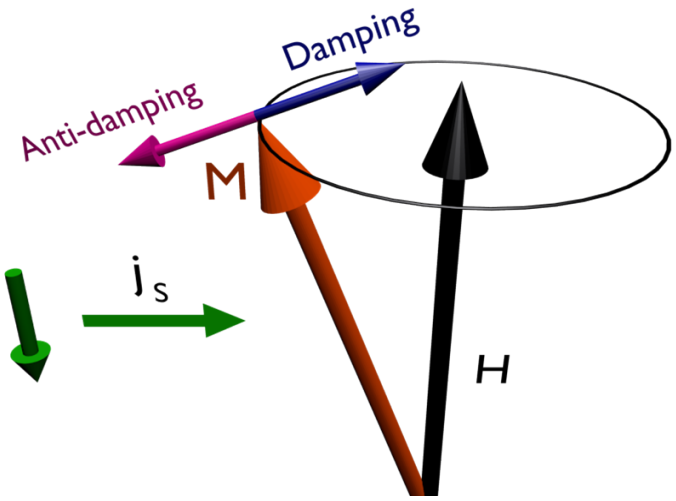

Figure 1.2: Precession of magnetization around an effective magnetic field with damping torques.

spin current available. The more important term for this discussion is the damping-like term, which depending on the sign of the spin polarized current can be used to either enhance or negate the internal damping of a ferromagnet[8–10]. This torque is the main contributor to controlling magnetization in the new generation of electronic spin based electronics.

The ability to tune the damping of a ferromagnetic material leads way to the creation of nanodevices called spin torque oscillators (STO). Going back to the mass on a spring analogy, if the damping of such a system is zero any oscillation will continue on forever. Moreover, if the mass where at equilibrium, changing the sign of damping will actually drive the system into oscillation. A STO is essentially a realization of this concept. When a large enough spin current is injected into a ferromagnet, its damping is reduced to zero resulting in a constant precession of the magnetization [8, 11–15]. The natural frequency of these devices is on the order of a few GHz, which is a typical frequency range used in current communications technologies.

Application wise, STO have a potential use in hard drive write heads through the concept of microwave assisted magnetic recording (MAMR). In MAMR a rf magnetic field can be used

to assist in switching of a nanoparticle [16, 17]. When the magnetization precesses in an STO, so does the magnetic field around the device which lowers the threshold for switching a bit on the hard drive. Recently, Western Digital has announced plans to incorporate STO into their hard drives, claiming that this will allow for potentially higher density of bits to be achieved.

Aside from an oscillating magnetic field, the electrical resistance of a STO oscillates as well. This arises from another property associated with magnetic materials and multilayer stacks, where their resistance changes depending on the relative direction of electric current flow and the magnetization. In the ferromagnet itself, anisotropic magnetoresistance [18] can lead to resistance changes. Bilayers of ferromagnets and materials with high spin orbit coupling can give rise to other effects such as spin Hall magnetoresistance [19] and unidirectional spin Hall magnetoresistance [20]. Structures containing two ferromagnetic layers separated by a spacer can give rise to even larger resistance changes through giant magnetoresistance [21, 22] or tunneling magnetoresistance [23, 24]. These resistance changes are then converted into a microwave voltage by the applied DC current used to create spin current. This results in a compact source of microwave power.

For the generation of a spin current, there are different methods that will be discussed here. The first is similar to the toy model presented earlier and deals with passing a current through a ferromagnet and into another. In this case, the internal field of the reference layer polarizes an incoming charge current and then is injected into a free layer. This method is used in many spintronic applications [2, 4, 8, 25] and so far is the most popular method for use in potential market products. For memory applications, the readout on a device like this can be understood again with a toy model. Figure 1.3a shows the modifications to the spin torque toy model, where the polarized electrons leaving the reference layer are passed through to the free layer. When these electrons enter the free layer there needs to be an empty state in the valence band for them to occupy. In a ferromagnet, the density of states

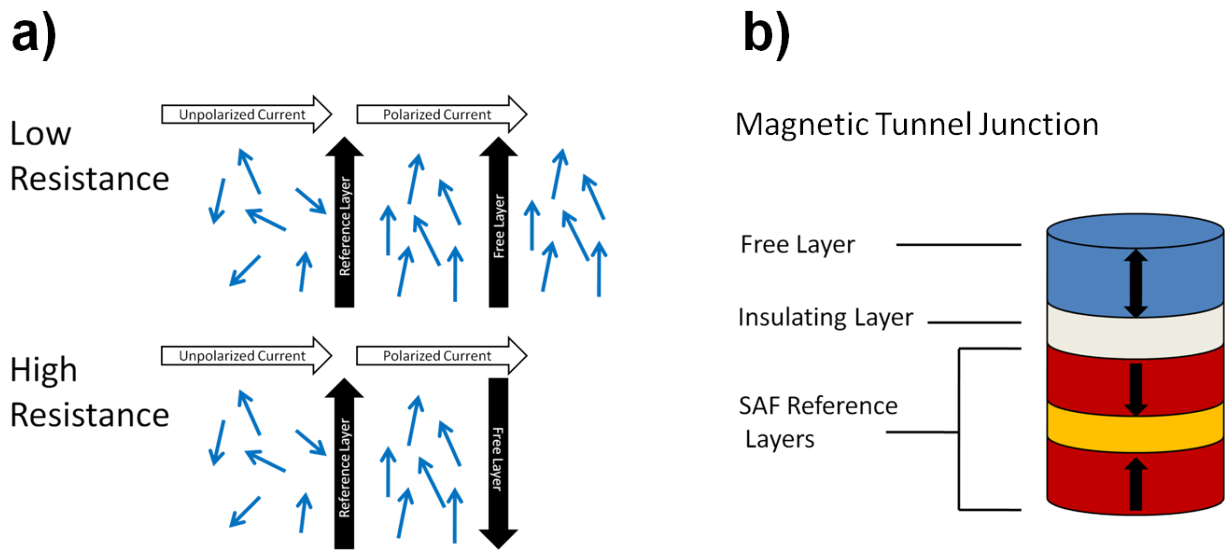

Figure 1.3: **a)** Toy model for the resistance change in two states of an MTJ. **b)** Simplified schematic for a magnetic tunnel junction.

for spin up and spin down electrons is shifted resulting in different transmission through the second layer. When the two layers are aligned, electrons are able to pass through whereas if anti-aligned, they are blocked. In reality, in the anti-aligned state there is still transmission, but the difference in resistance for the two states can reach over 100%.

One realization of this toy model is known as the magnetic tunnel junction (MTJ). A schematic of the basic parts of this device are shown in Figure 1.3b for a out of plane magnetized device. The free layer is the layer that is switched during the operation of the device and referenced to a fixed layer across a thin insulating layer. Usually CoFeB is used for the magnetic layers with MgO for the insulating layer [26]since these two materials band structures work well together. The magnetoresistance of this structure depends on establishing a tunneling current through the insulating layer. The tunneling probability is highly dependent on the relative orientation of the magnetic layers giving for a high change in resistance of the device and forms the basis for tunneling magnetoresistance (TMR).

Recently, interest has turned towards exploring other methods of generating spin current. One potential source is known as the spin Hall effect, which was first observed in semicon-

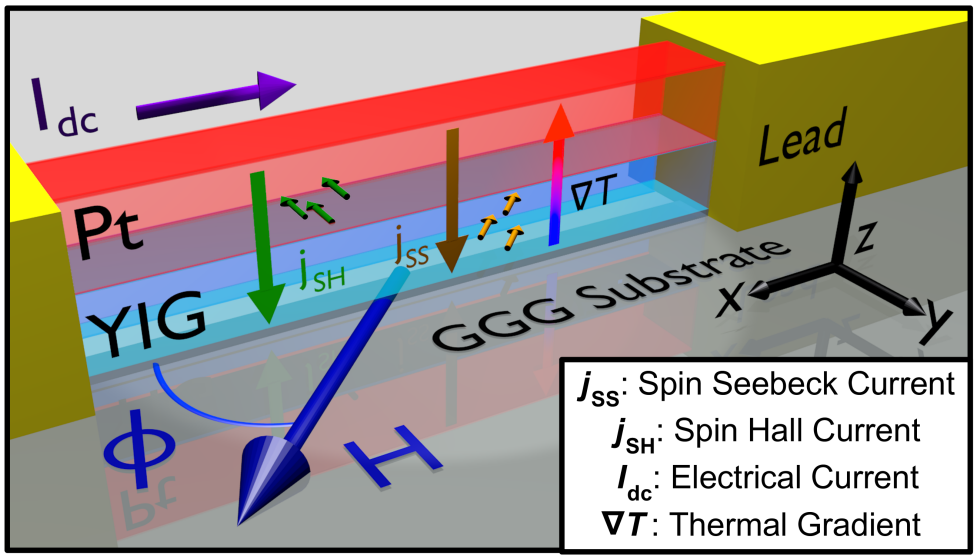

Figure 1.4: Model of a Pt/YIG nanowire based spin torque oscillator.

ductors [27]. However, in the early materials it was observed in the effect was too small to be useful. It was not until the observation of the giant spin Hall effect [5] in the metallic material Tantalum did this become a promising alternative. The spin Hall effect in these materials relies on the spin-orbit interaction present in heavy atoms, but conceptually spin Hall materials mimic the classic quantum mechanics problem of the Stern-Gerlach experiment. In a different rest frame, the orbitals of materials with a strong spin Hall effect resemble a magnetic field gradient. When a spin passes through this gradient, it is deflected in a direction that depends on the direction its spin had been pointing. If a ferromagnet is placed such that these currents are deflected into them, the result is a transfer of spin current into the ferromagnet. Figure 1.4 shows the resulting spin current generated from a spin Hall material such as Platinum being injected into a ferromagnet.

In this manuscript, the ferromagnet used was not always metallic. The insulating ferromagnet Yttrium Iron garnet (YIG) has gained popularity due to it having low magnetic damping. This allows for long distance propagation of spin waves and for studying the effect of spin currents that are not accompanied by a charge current. It has been shown in these materials that despite their lack of conductivity, they can still be manipulated by spin currents gener-

ated by the spin Hall effect [14, 15, 28]. Further, another potential source of spin current was found in these materials that becomes more apparent due to their insulating nature. Not only are they poor electrical conductors, they are poor thermal conductors as well allowing for the generation of large thermal gradients. If a structure similar to that of Figure 1.4 is made and a thermal gradient is produced as shown, a spin current flows perpendicular to the sample plane through what is known as the spin Seebeck effect [29]. This spin current is theorized to be carried by quasi-particles of magnetic vibrations, known as magnons[30–32]. The interaction of the magnonic spin current and the adjacent normal material results in the flow of a net spin current that depends on the direction the the thermal gradient. The magnetic damping of YIG has been shown to be tunable by the spin Seebeck effect in ferromagnetic resonance studies on films [33, 34]. Further, in nano-structures where large thermal gradients from Ohmic heating can be easily produced, the spin Seebeck effect has been able to drive auto-oscillations [15, 35].

Chapter 2

Experimental Details

In experimental research not every task that needs to be done is always scientific in nature. Often times an experiment will require the fabrication of new equipment. A large amount of time prior to the scientific work presented in later chapters went into the fabrication of the measurement station and related parts. Without many of these pieces, the measurements made would not be possible since commercial solutions are not always available or cost effective.

2.1 Cryogenic Measurement Station

The ability to manipulate bath temperatures provides several advantages over room temperature measurements. First, it reduces any noise due to thermal fluctuations making the measurement of low level signals easier. Second, due to the nature of the measured devices and the high current densities needed, their temperature can increase significantly (about 150K) over the bath temperature. For room temperature measurements, this means that the device temperature can start becoming close to the ferromagnet's Curie temperature or just

burn out. Aside from this, the properties of many materials are temperature dependent and being able to manipulate the bath temperature helps in determining if they are the cause of any observed effects.

The main component of the measurement station built here was a liquid helium cryostat manufactured by CIA industries with a temperature range of 1.5 K to 300 K. Figure 2.2 shows the engineering drawing for the cryostat with additional valves that were added on. The cryostat has two main chambers, the sample space and helium space. As indicated by their names, the helium space is where the liquid helium is stored and samples reside at the bottom of the sample space. A needle flow valve then allows for the flow of helium to the sample space. Since the cryostat works by allowing liquid helium to evaporate near the sample, a vent valve on the sample space allows for the gas to escape to atmosphere.

The fabrication of the station began with the assembly of the table to hold the cryostat. Making a sturdy table was important so that the station does not move and keeps the cryostat centered in the magnet. The older cryostat in the lab had a table that was bolted together and had a small amount of flex. To improve on this, a table structure was fabricated with welded joints and is shown in Figure 2.1a. The welder used was a Miller 211 MIG welder with a spool gun which does not make pretty welds on aluminum, but are structurally sound.

The next part of the fabrication involved building the support structure for the various valves needed to operate the cryostat seen in Figure 2.1b. These where made from aluminum and made on the mill in the machine shop. The then completed station is pictured in figure 2.1c. These valves are crucial to the operation of the cryostat. They can be used to pump on the sample space by closing the vent valve and opening the other valve on the line. A temperature of 1.6 K is then reachable with the valve to the roughing pump fully open and the needle valve mostly closed. For the project described in this study a temperature this low is not necessary, but for previous work on superconductivity it was important.

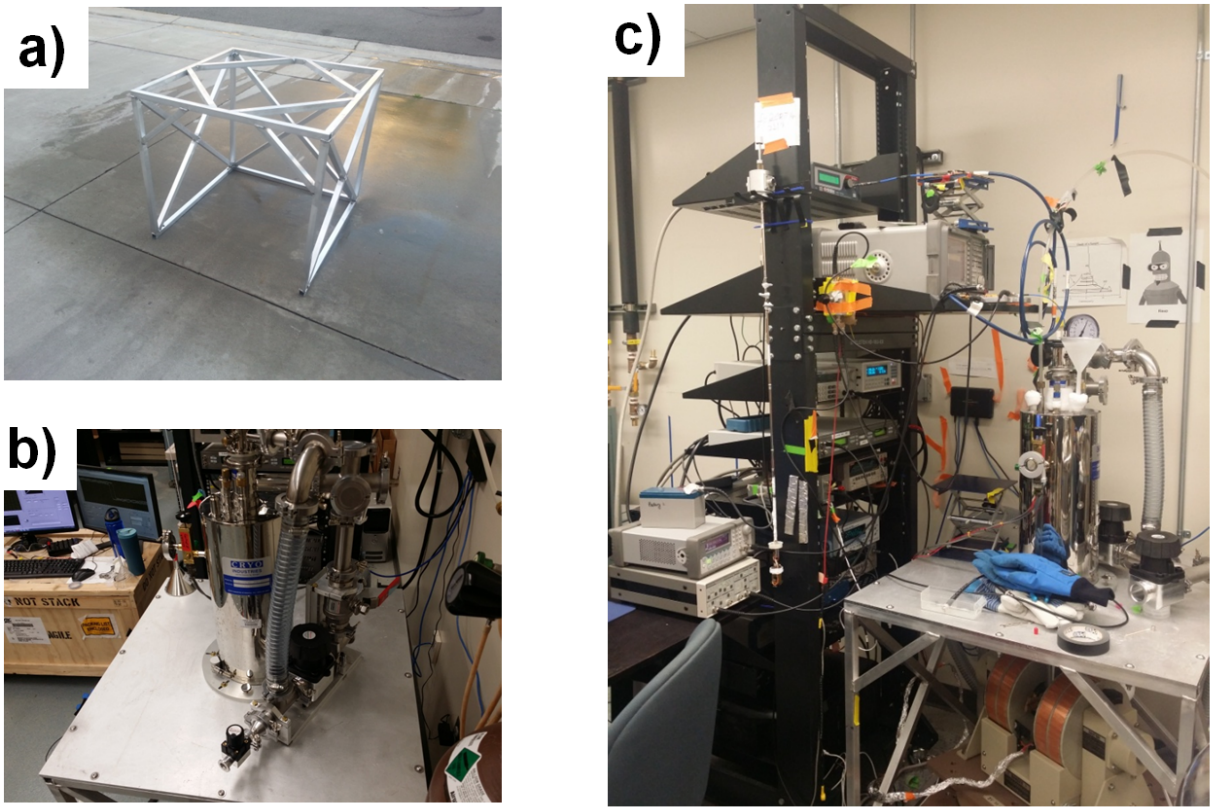

Figure 2.1: **a)** Support structure for the cryostat table. **b)** Valve support structure. **c)** Completed cryostation

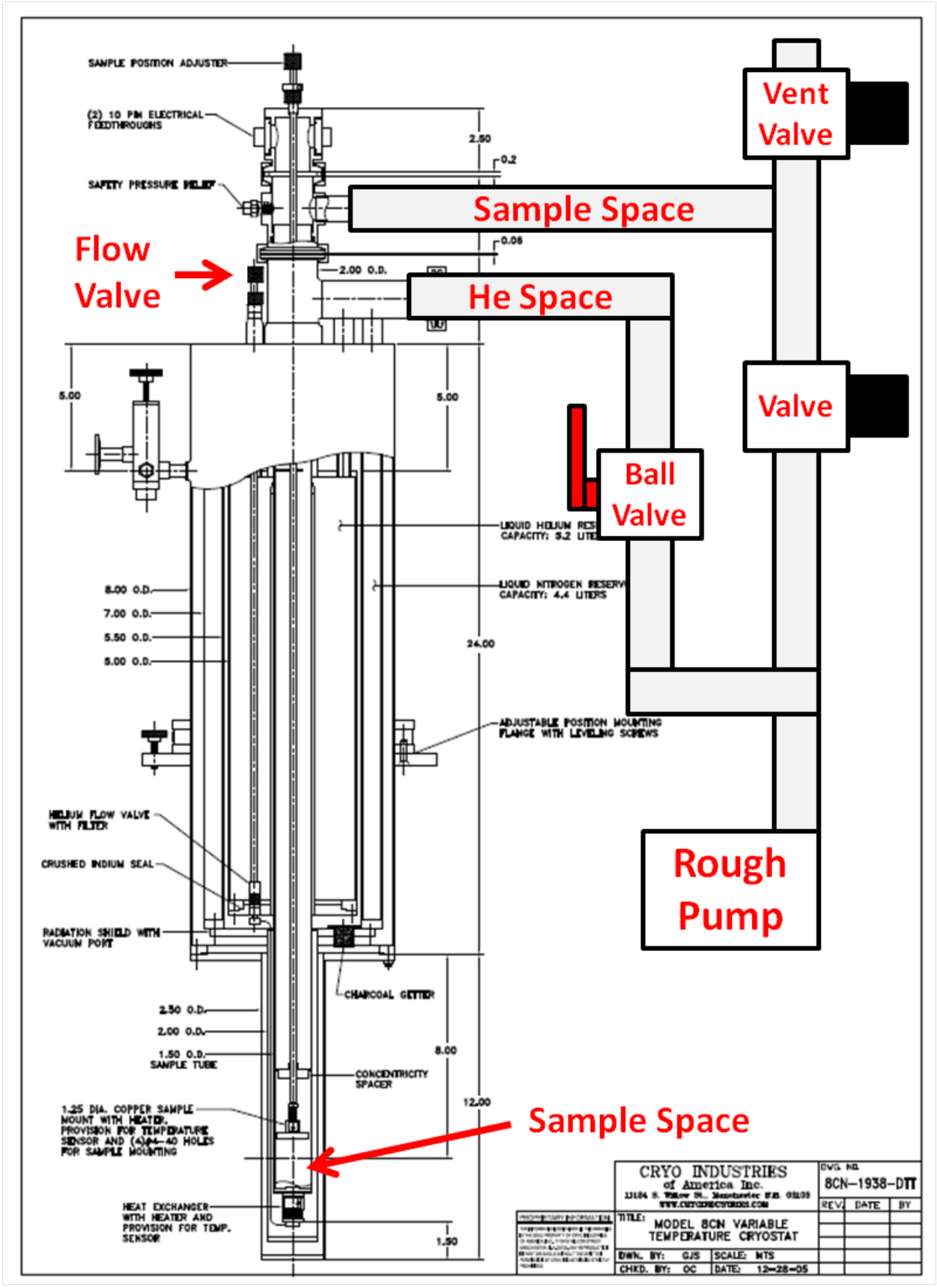

Figure 2.2: Schematic for the cryostat with the valve configuration.

The more important use of these valves is during the initial cool down of the cryostat. When the cryostat is not in use it is left exposed to atmosphere, meaning that air and water vapor are inside the system. In this state if liquid helium were to be transferred in, all these gasses would solidify and block the flow of helium. As such, the chambers need to be pumped out. The general procedure is to use these valves to pump each chamber individually for 15 minutes. Then usually I fill the spaces with He gas and pump once again to flush the cryostat. If the cryostat has been sitting for a while I will repeat this procedure a few times.

After flushing the cryostat at room temperature, the nitrogen jacket is then filled with liquid nitrogen to start cooling the system. The main purpose of this jacket is to insulate the liquid helium, however the cryostat can be cooled to 100K with just the jacket. Pre-cooling the cryostat like this is not completely necessary, but less liquid helium will be wasted during transfer since the chamber is closer to 4.2 K.

The most common problem with cooling down the cryostat or transferring in liquid helium is freezing the flow valve internally or externally. Freezing on the exterior is relatively simple to fix by using a heat gun to melt the ice on the brass knob. If the knob still refuses to turn, a pair of pliers can be used to free it. Generally rocking the valve left and right gently works for this. Internal freezing of the capillary is the other potential failure point. The sign of this is usually the flow valve knob turns, but the cryostat will not cool. There is a heater on the flow valve placed there for this situation. Applying heat to the capillary can some times free it up. However, this is risky since it operates in open loop and if too much heat is applied it can possibly melt the solders and damage the cryostat. I would not recommend using this too often.

In theory the cryostat can be operated using only liquid nitrogen. This was attempted early in the project but seemed to have caused damage to the cryostat. Inside the helium space there is a mesh grating that ended up getting plugged, requiring the cryostat to be sent back to the manufacture for repair. The clog was caused by a black residue. Although the exact

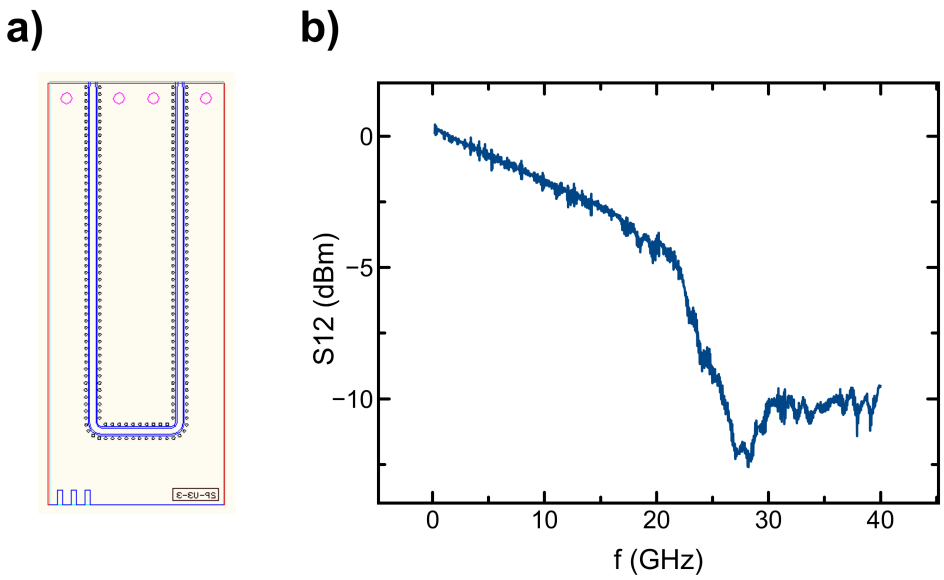

Figure 2.3: **a)** Drawing for a U shaped waveguide. **b)** S12 parameter for the waveguide.

origin of this residue is unknown, it is highly likely it came from the liquid nitrogen since it is not completely free of contaminants.

2.2 Coplainer Waveguide Design

Most of the measurements that will be described in this study require the transmission of microwave power. The frequency range used spans from 1-20 GHz, in which currents behave differently than DC. Microwave currents act more like waves with the possibility of various circuit resonances that can affect the propagation of microwave. Due to this, the design of the waveguide needed to send current is important. A typical waveguide has a central line with a ground along it at all times. Conductive holes, called vias, are placed in the ground pad along the central and serve to build a wall for the microwave and increase the frequency bandwidth.

Since the experiments done in our lab are not exactly industry standard, special waveguides needed to be built. The design for the waveguides was based on the Southwest design [36]

and configured specifically for our setups. Figure 2.3 shows a design for a CPW meant for conventional broadband ferromagnetic resonance measurements on films and its transmission characteristics.

2.3 Sample Holder

Microwave waveguides with a design similar to the one in the previous section are not what is needed for use in the cryostat most of the time. The YIG based nanowire samples measured here need a field that can be rotated in the the sample plane. Due to the geometry of the cryostat and magnet, this requires building a holder where the microwave makes a 90 degree turn. Since microwave currents act as waves, the bends cause reflection points and ultimately develop transmission characteristics that are highly frequency dependent. Work addressing this problem was done with 3D printed holders, since this fabrication method provides for a fast turn around.

The final design is the partially assembled holder seen in Figure 2.4a. These are made from brass that is cast into 3D printed wax molds by Shapeways. The waveguide used is the same design as the previous section and the central line is later cut to the length needed to fit whatever sample is measured. The holder has a cap shown in Figure 2.4b to catch a sample if it falls off the waveguide.

This particular design has decent transmission characteristics up to 15 GHz as illustrated by Figure 2.4c. Even up to 40 GHz, its attenuation is not too high, but there begin to be several resonances. The main problem with the design seems to be related to where the central pin of the Southwest K connector is soldered to the waveguide. In the early designs, where the central had to extend farther away from the ground, the resonances were worse. Modifying this connection would likely increase the quality of the holder, but for the frequency range

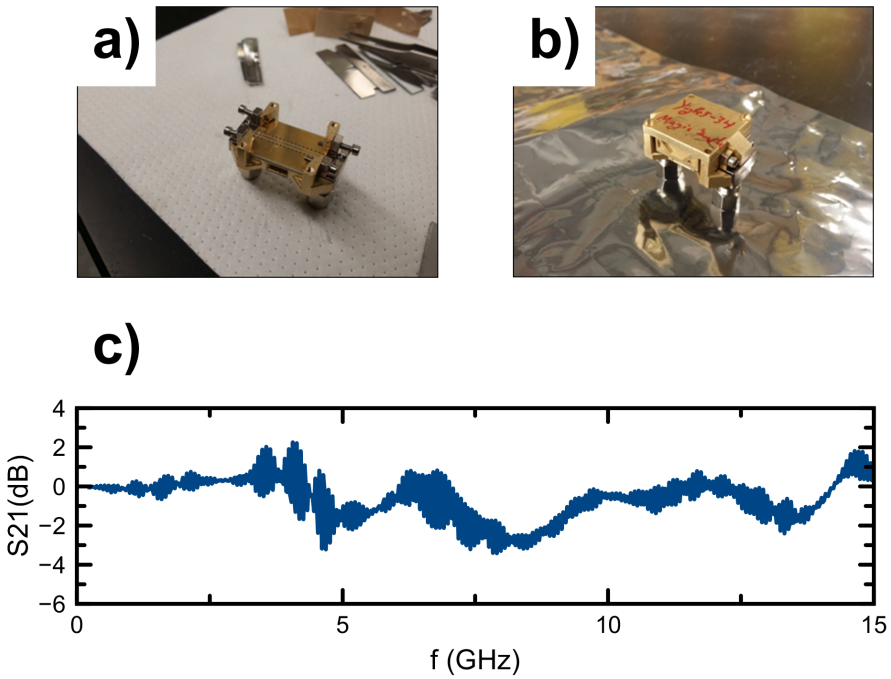

Figure 2.4: **a)** Microwave holder during construction. **b)** Completed holder with cap installed. **c)** S12 parameter for the holder.

used in this study it is adequate.

2.4 Low Noise DC Current Source

Although many of the measurements made rely on the microwave properties of the samples. The main interest in this study is to observe the change of these behaviors from the addition of an extra DC spin current. To improve signal quality it is very important that the DC current source be as clean as possible. Current sources such as Kiethley 2400s and Yokogawa GS200s claim to be low noise, but for the low level signals that will be measured here are not sufficient. Typically there are different current ranges on these sources and the noise observed is directly related to the range used. For the lowest range the noise is the least and it is possible to obtain a decent signal, however, does not provide enough current for this study. Ideally this noise can be eliminated by decoupling the digital electronics from the DC

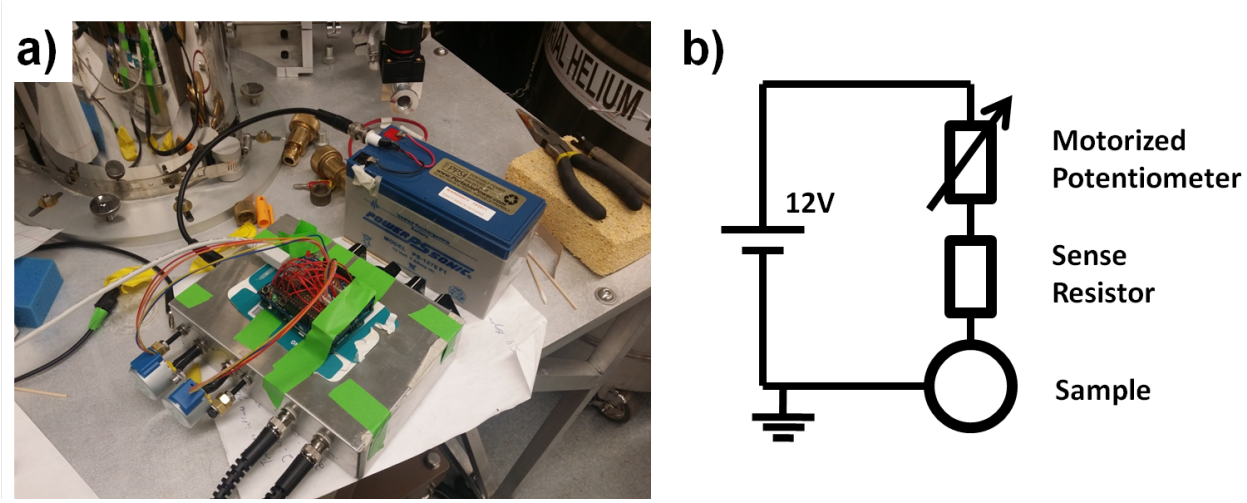

Figure 2.5: **a)** Battery based DC current source **b)** Equivalent circuit diagram for the DC current source.

side.

A decent solution for decoupling the digital electronics and making a low noise current source is surprisingly the simplest imaginable way of varying the current thorough a resistor, a voltage divider. A 12V battery provides for a very stable low noise voltage source. By placing a variable resistor in series with the measured sample the DC current can then be varied. The samples used in this study have small percentage changes in resistance, so the current provided by this divider is relatively constant. The biggest drawback to this method is if the study being performed is a DC bias study, the grad student performing the measurement gets very tired of turning a knob every few minutes very quickly. The solution to this was to use an arduino and stepper motor to allow computer operation. The use of a mechanical control decouples the digital electronics from the DC line preserving the low noise qualities of a battery source. The motor is secured to the knob with tape in a way that allows some give in case the motor vibrates slightly when powered.

Figure 2.5 shows the actual current source and a schematic of the DC circuit used. Feedback for the current value of DC current is achieved by placing a sense resistor in series with the sample and monitoring the voltage across it with a low noise voltmeter. Sadly the inclusion

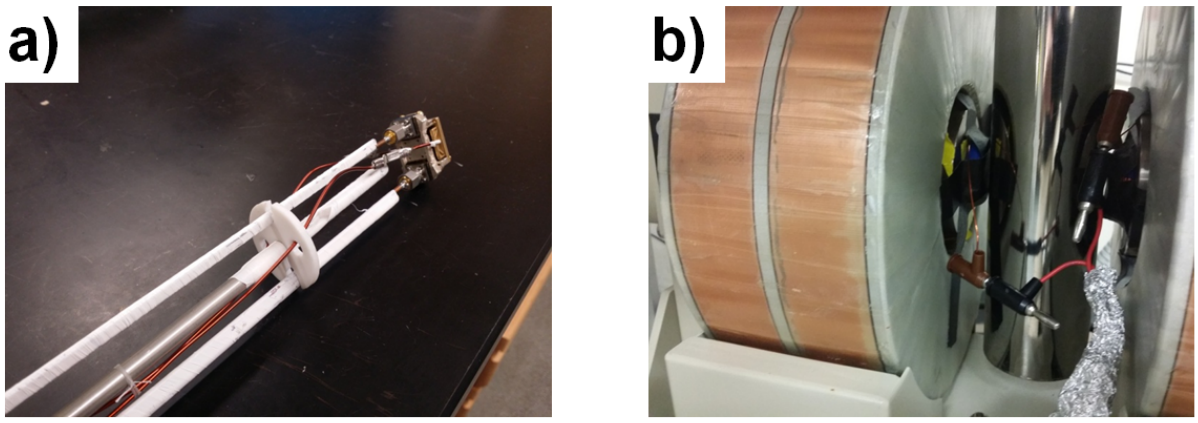

Figure 2.6: **a)** Early prototype sample holder with single wire used for modulation **b)** External modulation coils placed outside of the cryostat

of a voltmeter increases the noise level slightly, but the remote control makes up for it. Running the current through an ammeter was tried as well, but the ammeter introduced far more noise than the voltmeter.

2.5 Field Modulation Coils

The measurement techniques presented in the next chapter rely on the ability to generate a AC magnetic field in order to create a modulation for lock-in detection. There are several experimental details that help improve signal quality. In general any little bit of improvement that can be made to the setup is worthwhile since it decreases the amount of averaging needed, and consequently the total measurement time needed. The design and implementation of the field modulation can change the quality of the signal. Even ignoring the design, not all modulation frequencies give the same noise level. It is usually best to optimize the modulation frequency by sweeping it and measuring the noise present.

Adding field modulation to the cryostat is not a completely simple task. The geometry of the cryostat restricts the possible designs and if the coils are placed outside the cryostat, the

cryostat's metal attenuates the modulation. Early designs for the setup used a single wire placed in the cap above the sample holder as seen in Figure 2.6a. For a long time in the lab's probe stations, the use of a single wire with a high current of roughly 4 amps had been a proven successful method. However, implementing this into the cryostat did not share the same success. Mainly this is because once installed, the direction of the wire could not be changed. This is problematic since in order for field modulation to work properly, the modulated field direction needs to match the applied field. Secondly, running 4 amps current through the cryostat seemed to increase the helium consumption and occasionally the wire would short on the sample holder cap, resulting in death of the sample.

The best solution was mounting external coils outside the cryostat like in Figure 2.6. Surprisingly a small modulation frequency of 267 Hz still works even though one would expect the amount of metal in between to block some of the AC modulation. The signal quality from such a coil was found to be similar the wire when the wire's modulation field was aligned with the static applied field. However the modulation from a single wire decreases as the field is rotated where the coils do not. One issue with the external coils is they will tend to vibrate in a strong magnetic field. Aside from producing a loud audible noise, a vibrating coil will cause the AC modulation to have a distorted waveform introducing electrical noise. Since the vibrations depend on the strength of the static applied field, it introduces an additional field dependent background that is often not a simple function.

The early coils were made from wire wrapped around round plastic sample holders. These were taped to the pole pieces and often required cardboard to be jammed between them and the cryostat to keep them from vibrating. While this worked, it was far from ideal. A better approach was made using a 3D printer to design a sleeve that fits over the magnet pole piece. This sleeve had indents patterned into it to hold the modulation wire as shown in Fig. 2.7a. After wrapping wire into this sleeve, electrical tape is tightly wound around it and then it is inserted onto the magnet pole piece. Figure 2.7b shows a completed coil.

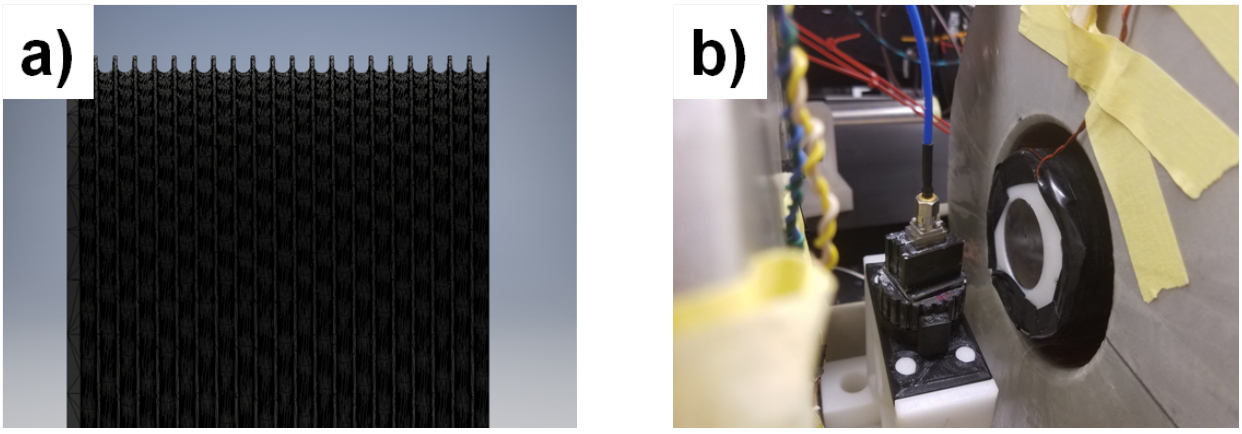

Figure 2.7: **a)** Side view of a 3D printed modulation coil. **b)** Assembled exterior modulation

Chapter 3

Nanofabrication

Nanofabrication is the process of patterning nanoscale devices using a variety of techniques that boil down to additive and subtractive processes, where material is either added or removed. In principle, the basic ideas behind the processes are often simple, however there is a certain degree of finickiness to the process recipes and equipment making it more difficult than it seems. As such, there is a level of patience and persistence needed to complete a process since failure is a guaranteed part of the process. Often times several parts of a recipe may end up being superstition since the time required to fully test is prohibitive to reaching the ultimate goal of a completed device. In this chapter I will detail the process used to fabricate the nanowires patterned in this study.

Before going into details of the procedure which will be discussed in the following sections, the general overview of the process used to make YIG/Pt nanowires is illustrated in Figure 3.1 and an itemized version is available in the Appendix. First staring from YIG/Pt films, alignment marks are patterned by using a lift off procedure. These serve to align the multiple steps in the process and locate the center of where a device should reside and without them, it would not be possible to properly attach the electrical leads to a nanowire. Next using a

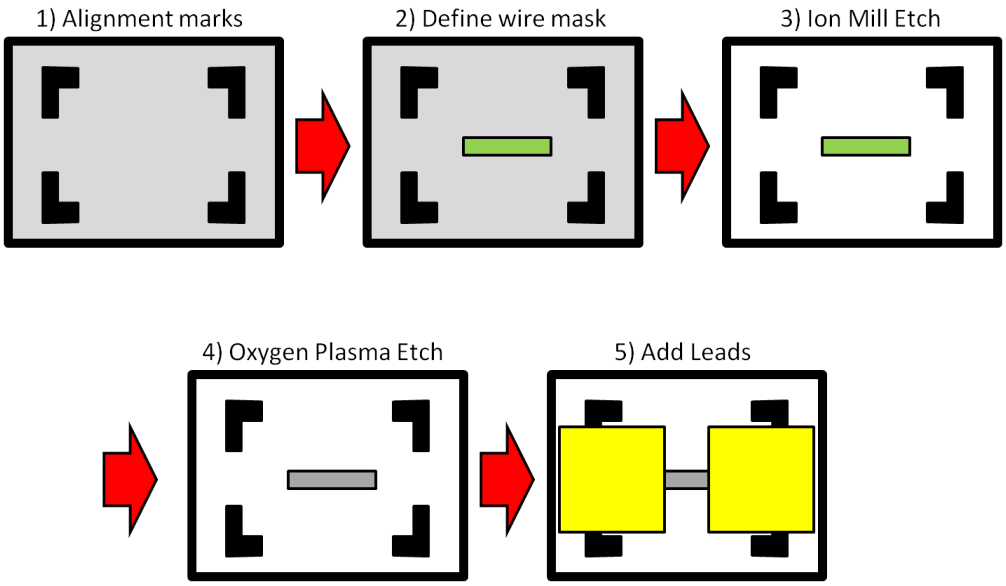

Figure 3.1: General process flow for the fabrication of nanowires used in this study.

negative resist MAN-2401, the outline of the wires is defined. Then an ion mill is used to remove material leaving only the YIG/Pt under the remaining resist. In order to make a good electrical contact to the wire, the resist is removed using oxygen plasma etching. Lastly electrical leads are added using a lift off based procedure.

3.1 E-Beam Lithography

The process used is heavily dependent of a technique known as e-beam lithography. In it a resist is spun on to the chip and then using a modified scanning electron microscope (FEI Magellan in this case), areas of the resist are exposed to the focused electron beam. This beam is then rastered across the substrate to create a pattern. If a positive resist such as PMMA is used, the area exposed to the electron beam can then be developed to expose the substrate where the beam had been passed over. On the other hand for a negative resist such as MAN-2401, the exposed area remains after development. This process creates the necessary masks that will be used to add and remove material. Details of the resist

application procedures are detailed in Appendix A.

The writing process on the Magellan SEM is run by the Nanometer Pattern Generation System (NPGS) software. NPGS is a fairly widespread and older program that while it can get the job done, there are often various communication errors between the separate NPGS computer and the more modern SEM. These errors can be reduced by the resetting some of the related components every time. The whole procedure wastes a small amount of time, it is much less time than the failure of a three hour write session. To reset everything, first stop the server on the SEM. Once the server is shut down, restart the EBL computer. Before logging into the EBL computer, make sure the server on the SEM computer is started again. Then logging into the EBL computer will initiate some sort of calibration between the SEM hardware and NPGS computer. Once the calibration is completed, log into the NPGS before imaging on the SEM or else occasionally when you log into the NPGS software it resets the SEM settings, which can undo any nice focus it currently had.

The beginning of the writing procedure requires first the ability to make a decent image with the ETD detector at a working distance of 7 mm. The tricky part is this has to be done with the conditions the EBL writing will use, forcing the beam voltage to be set to 30 kV and the desired write current. The current used will vary depending on the size of the feature, but generally the smaller the feature the lower the current is used. Sadly though the conditions used for writing do not produce good images so getting a good focus can take time on more insulating substrates. For larger features, the focus is not as important and often all that is needed is a rough focus, but for small features where the dimensions and aspect ratio matter, proper setup of the SEM is critical. The general rule of thumb is an image of a feature the size of the write pattern should be in good focus at least. To aid in the focusing process, scratching the side of the chip creates dust particles with jagged edges. The sharper the feature the better since it is easier to observe any problems with the focus, stigmator, and all relevant alignments.

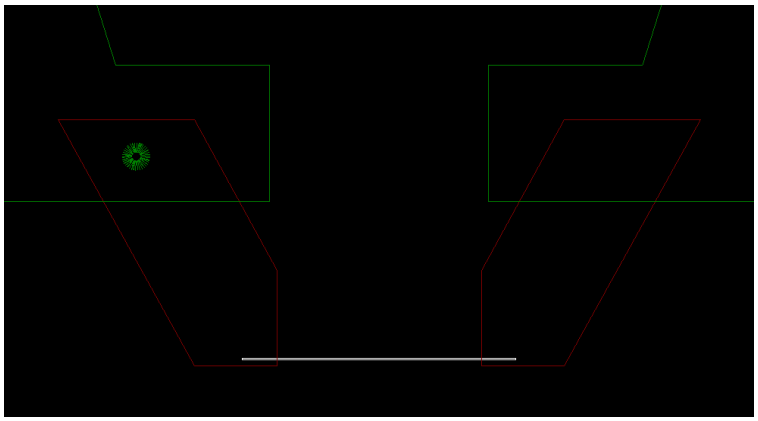

Figure 3.2: Example of a pattern file with the dump point added (green circle)

Now that the SEM is prepared for the writing session, it is time to turn to the details of the pattern file and the run files. Ideally these would be prepared ahead of time since not only is SEM time hard to get at decent hours due to its popularity, tool use has an hourly fee so being efficient with time is strongly encouraged. The patterns for the runfiles are in dc2 format and are intended to be written in the drawing program included with NPGS, but drawing with this software is difficult. Instead Layout Editor is much easier to use and the gds files it saves in can be converted to dc2 by NPGS.

After converting the file to dc2, there needs to be the addition of a dump point in the NPGS pattern drawing software. The purpose for this is when the beam is not writing, the software points the beam at this location. This is mainly intended for SEMs without beam blanking capabilities, but the blanker on the Magellan does not always work properly leaving behind a dot in the center of the pattern. When placing the dump point it is best to place it away from the main pattern or inside a large feature like the pattern in Figure 3.2.

Once the pattern is ready, the runfile as pictured in Figure 3.3 can be created. There are several parameters that can be varied and also changed for different layers in the pattern. Generally the best parameters will need to be tested for each new type of pattern. However, there are a few general trends. The first parameter of interest is the Magnification. While I actually do not know the exact function of this, the smallest value you can input into this

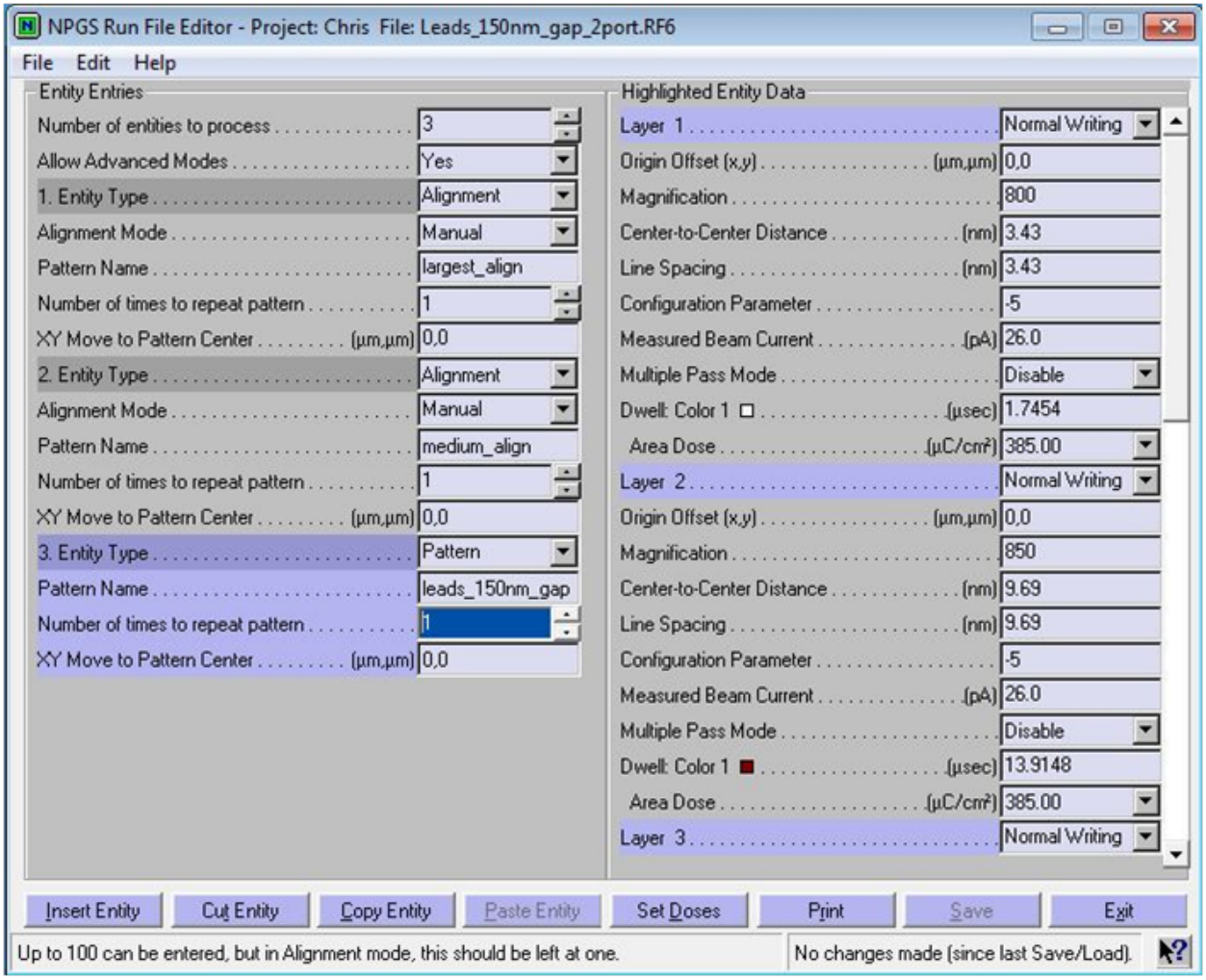

Figure 3.3: Sample runfile for the NPGS software.

field before the software complains gives the best result. The center to center distance and line spacing govern the distance between points where the beam will expose and setting these to the same value works best. The value used here will depend on the size of the feature and the current used. The beam size is related to the current used so for lower currents, a smaller distance between points is needed. Also for smaller features this helps with their resolution. The write current is selected by the configuration parameter setting. This is an old convention where the number means the current list entry number referenced to one of the list entries. The measured current value allows for a correction that takes into account the actual measured current with a Faraday cup. In principle this can just be set to the selected current and the dosage varied to make the pattern work right.

The dosage governs the final amount of exposure to the electron beam. There are two different dosage schemes that can be used and throughout this study the "area dose" scheme was chosen. The amount of dose used needs to be determined experimentally when starting a project by writing an array with varying dose steps. For PMMA and MAN-2401 a dose around 300 works well for most larger features. For features under 100 nm, especially nanodots, the amount of required dose can be significantly higher.

3.2 Film Deposition

The Yttrium Iron Garnet thin films are prepared by collaborators at Colorado State University using sputtering techniques [37]. Gadolinium gallium garnet (GGG) is used as a substrate due to its good lattice match with YIG. Platinum is then deposited at room temperature in the sputtering chamber located in our lab. Just prior to the deposition, the stage bias is used to perform a light argon cleaning of the surface for 20 s at 40% power.

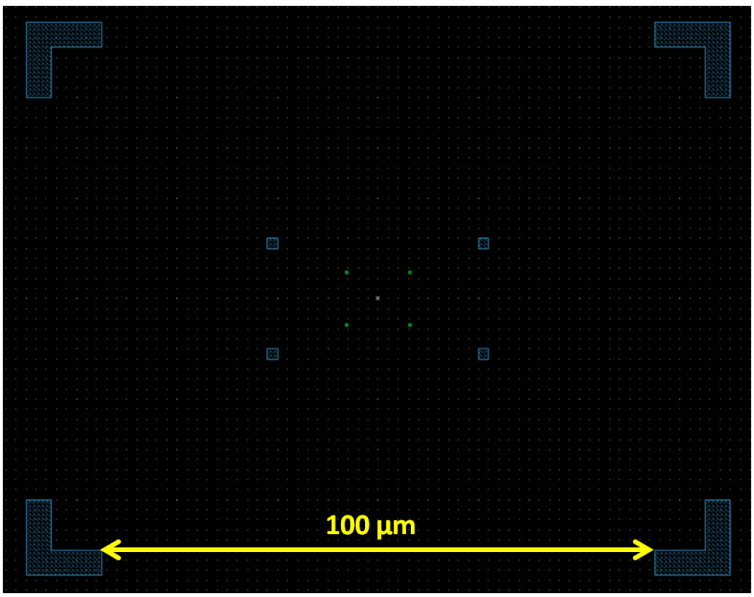

Figure 3.4: Pattern for the alignment marks used

3.3 Alignment Marks

Alignment marks provide the important role of allowing subsequent e-beam lithography steps to be aligned to the same location. The NPGS software used for patterning allows for imaging specific areas before writing a pattern. By creating an outline of the alignment mark in the run file, one can move this outline over the imaged alignment mark. The software then uses this to calculate where the center of your pattern is. A general rule of thumb is the closer to the pattern center the marks are, the more accurate the placement of features can be.

Figure 3.4 shows the typical alignment marks used in this study. The outer, larger marks serve to provide an easy to locate feature for a rough alignment. After the first alignment, the final alignment is done using the middle alignment marks. It is important that when doing the alignment, the current is set to the same one as the write current. Often there is an offset in location for different currents. On the pattern there are one more level of alignment marks for an even finer alignment and give an accuracy of about 15 nm in placement. Figure 3.5 shows an SEM image of a nanodevice made for a different project using the full alignment,

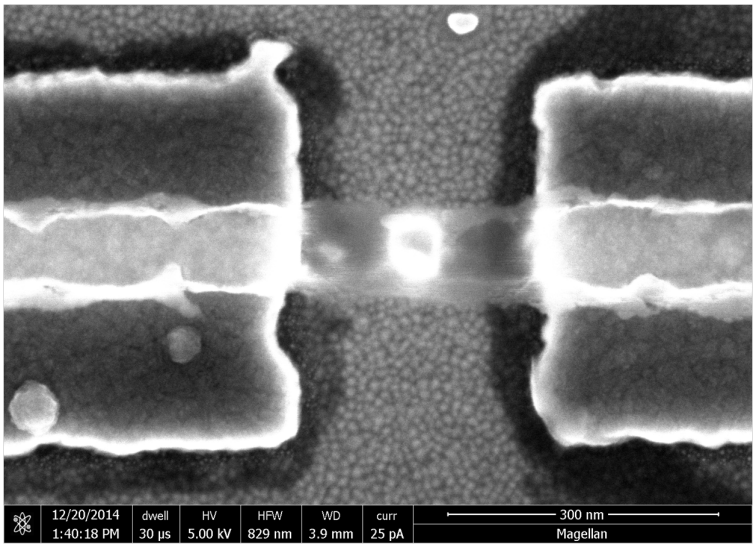

Figure 3.5: SEM image illustrating the level of alignment that can be achieved using the alignment marks, where a wire is written over a nanodot at the center of the image.

where a wire runs over a nanodot of another material at the center of the image. However, for the type of patterns made in this study, this level of accuracy is not required so these marks where not used.

The alignment marks are written in an array into MMA/PMMA resist. The details of the resist development are in Appendix A. Then material is deposited onto the chip. In principle the material used is not too important and just about any metal that will adhere to the chip's surface material will suffice. 30 nm of Tantalum seems to work well for alignment marks and has the benefit of being a relatively cheap material.

3.4 Wire Definition

Next the YIG/Pt wires are defined. A subtractive process involving ion milling was used due to the nature of the YIG/Pt thin film growth. Since high temperatures are needed to anneal the YIG layer, a lift of procedure can not be used since the high temperatures would bake the resist and make lift off difficult. Further, lift off procedures tend to make sidewalls

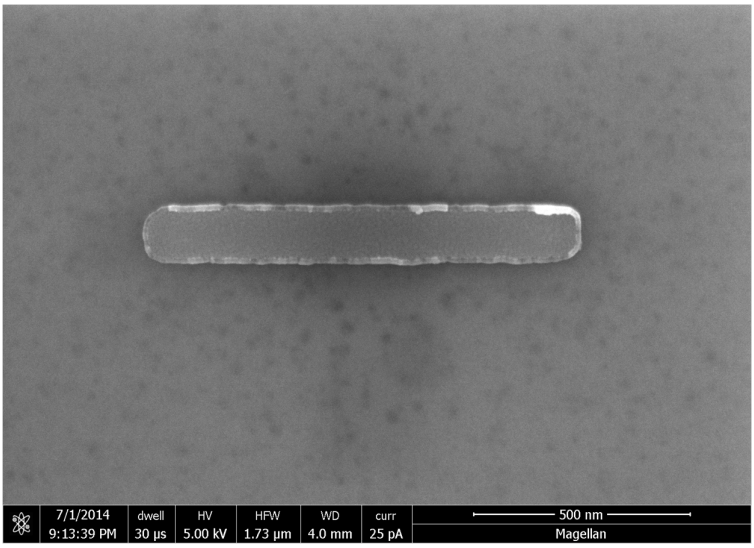

Figure 3.6: SEM image of a lift off defined nanowire showing the sidewalls around the edge of the wire.

made from the same material as the wire, which can be seen as the bright edges in Figure 3.6. These magnetic sidewalls often become oxidized when exposed to air, and in the case of metallic ferromagnets, these oxides are often anti-ferromagnetic at low temperatures. Even just small amounts of oxides can alter material properties [38], so it is not surprising that large sidewalls can result in unpredictable behavior at low temperatures and are best to avoid.

The first step in the subtractive process is to create a mask that will define the wire. Traditionally in our particular lab this has been made from materials such as chromium or alumina via a lift off EBL procedure. The thickness of these masks is calibrated such that very little to none remains when the ion milling step is completed. However, for these YIG/Pt wires there are problems involved with this method. YIG etches relatively slowly and is much thicker than in previous nanowire devices made. This would require then a hard mask that is too thick to be feasible.

The first approach for a hard mask was to use a hybrid of HSQ and PMMA resists[39]. HSQ is a negative resist that when developed, forms a material similar to silicon oxide. Its

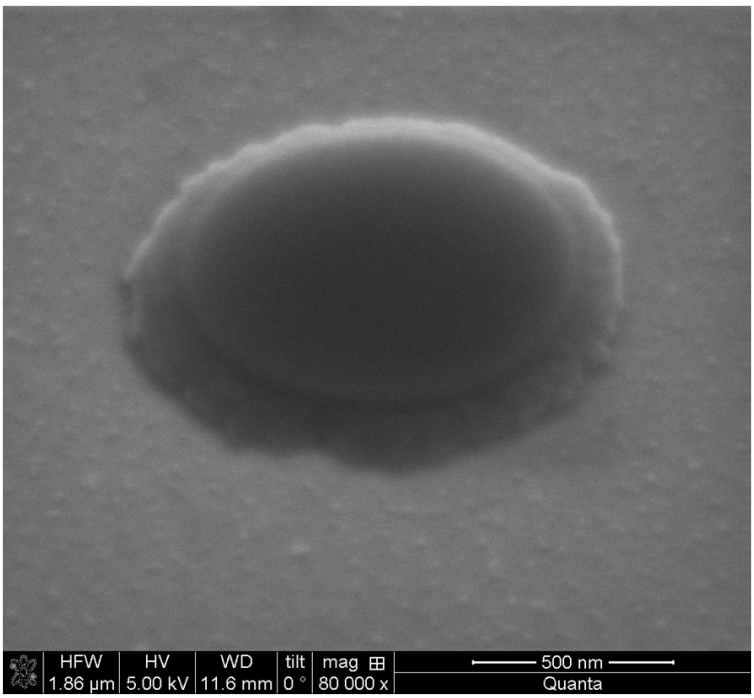

Figure 3.7: SEM image of a one micron circle of PMMA after a HSQ mask was transferred to it.

etching rate is too fast to be used as a hard mask for the creation of YIG/Pt nanowires, so another material needed to be used to increase the etch time. Further, the resultant silicone oxide can not be easily removed. A method was used where first PMMA is spun followed by HSQ using the recipes in appendix A. After writing and developing the HSQ, the pattern can then be transferred to the PMMA with oxygen etching since it does not etch the HSQ, leaving the PMMA intact underneath the HSQ mask. The remaining PMMA is then plenty thick to survive the ion mill etching step. This method however did not give the desired resolution as seen in Figure 3.7. Even though the very top HSQ layer in this 1 micron circle is well formed, the pattern transfer to the PMMA layer is poor. This may not necessarily be a problem with the concept since it has been shown to work [39], but rather the tool used. For the oxygen etch a Harrick O2 cleaner was the only tool available and is primarily meant for cleaning surfaces, not a nano-patterning step.

A procedure using a negative resist MAN-2401 as the hard mask was then attempted. MAN-

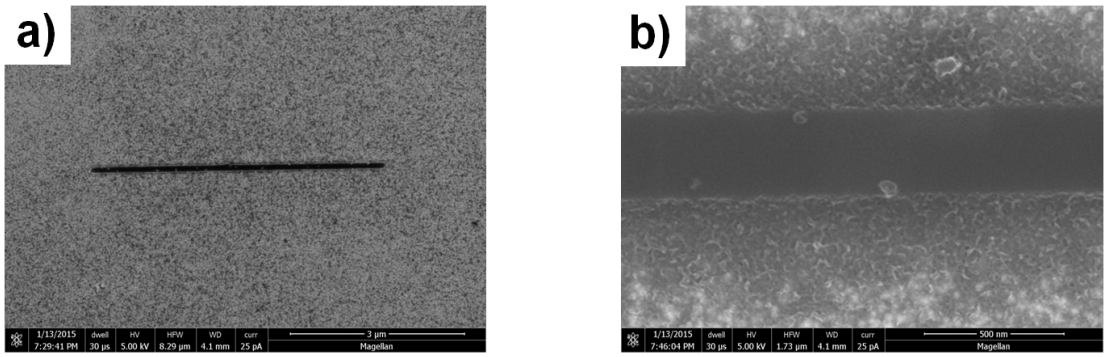

Figure 3.8: **a)** Negative resist mask for a nanowire before etching. **b)** Excess residue next to a bad nanowire.

2401 is spun using the recipe described in Appendix A. One important thing to note is MAN-2401 is UV sensitive so exposing it to ambient light for too long can develop the entire chip. The resist is then patterned into wires using e-beam lithography. The exposure characteristics for this resist are similar to PMMA but requires slightly less dosage. This is convenient for protecting the alignment marks from the etching step since the imaged area during alignment is usually developed. After the exposed areas are developed, we arrive at the completed nanowire in Figure 3.8a.

Often times there is a resist residue present as the edges of the wire seen in Figure 3.8b. During the testing of the negative resist fabrication process this was never seen and only seems to happen on thin Pt layers placed on a fairly insulating substrate. The early testing was done on a thick Pt layer so is not likely to be related to the resist adhesion to the Pt. Since this only happens with thin Pt, it is probably due to the higher resistance of the thin Pt layer not dissipating the writing beam's charge fast enough. More testing would be needed to verify this. However, the residue at the sides appears to be thin in comparison to the remaining resist mask so by etching for an excessive time, the nanowire shape can be preserved.

Next an ion mill is used to transfer the resist pattern into the film. The MAN-2401 mask is roughly 100 nm tall so in order to reduce shadowing, an etching angle of 65 degrees is used,

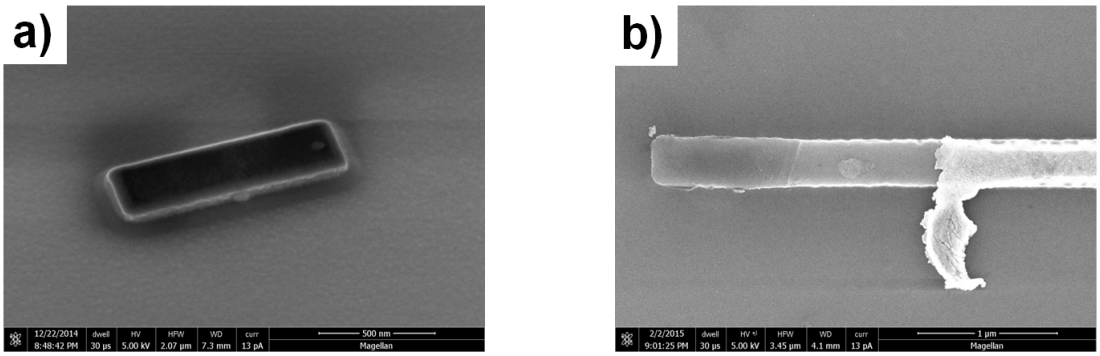

Figure 3.9: **a)** Baked on resist after an ion milling step. **b)** Partially lifted off MAN-2401 resist using acetone.

where the angle is between the ion beam and sample plane. YIG etches slow (3.7 nm/min) and since the layer is relatively thick, a long etching time is required. The etching process creates unwanted heat at the sample and tends to bake on the resist. Figure 3.9a shows an image of baked on resist from the early testing of the MAN resist etching characteristics using Pt on silicone substrates. After the initial testing a duty cycle of 25 percent was used to try and reduce the heating, but still results in baked on resist. The main thing to take away from this image is that there is still resist present after a long enough etch to define a YIG/Pt wire.

After the milling process it is then necessary to remove the negative resist to allow for the electrical leads to make contact to the surface of the wire. According to the datasheet for MAN-2401, this can be done with acetone but the remaining resist is usually too thin and baked on for this to be a possibility. However, for etching thin metals this can sometimes work. The resist seems to remove in chunks with acetone rather than being dissolved away as shown by a partially lifted off bit of resist in figure 3.9b. In theory it may be possible to lift off a thicker negative resist with acetone, but this approach was not taken since a thicker resist will create more shadowing. To remove the remaining resist oxygen plasma etching was used with a Harrick O2 cleaner. A nine minute etch with this tool set on "High" was enough to completely expose the Pt layer giving the completed wires in Figure 3.10.

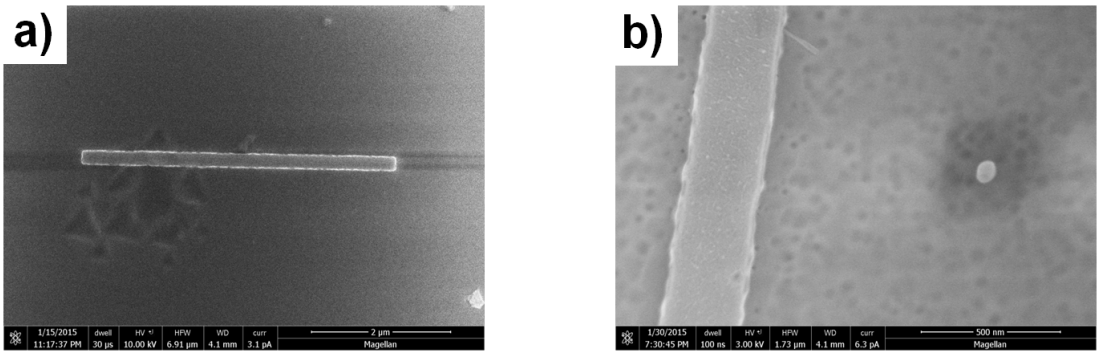

Figure 3.10: **a)** Completed nanowire after etching and with resist removed **b)** Zoomed in image of a completed nanowire showing full resist removal

3.5 Lead Definition

The last part of the process is the attachment of electrical leads to the nanowire through a lift of process. First, a layer of the positive resist MMA is spun on the sample using the recipe listed in the Appendix, followed by a layer of PMMA. MMA is affected by the electron beam more than PMMA, resulting in an undercut in the resist as illustrated in the side view of Figure 3.11. This aids in lift off of sputter deposited films.

The substrate used, Gadolinium Gallium Garnet, provides some challenges for the e-beam lithography process because it is insulating enough to create charging problems during the writing process. Since the writing current can not be dissipated, the charge buildup begins to deflect the writing beam causing the pattern to distort, often enough to where it is not usable. To combat charging, a thin layer (1-2 nm) of Pt is deposited on top of the PMMA layer. This provides a conductive channel to remove excessive charge and is thin enough to not disrupt the development of the underlying resist.

The lead material for the devices was initially based on Ti/Au multilayers. Generally Ti is a good adhesion layer for oxide materials but did not seem to adhere well to the GGG substrate. Near the wire the leads would often be torn and wire bonding to the pads was difficult. Imaging the leads after development reveals part of the problem. Figure 3.12

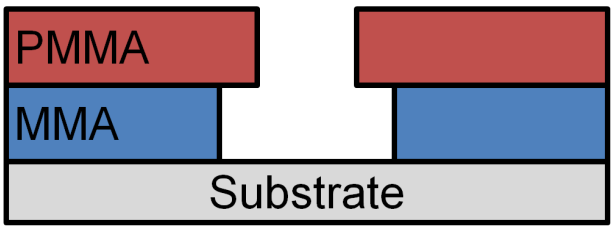

Figure 3.11: Side view of a trench made in a MMA/PMMA bilayer.

shows that the Pt layer on top of the PMMA sometimes does not break apart during the development process and falls down to the substrate. This then prevents adhesion of the leads. In initial testing of this process this was not an issue, but the process of Pt breaking up is likely very sensitive to the Pt thickness. Over time deposition rates in a sputtering system will vary slightly and it is likely the Pt layer is thicker than desired.

To try and account for any remaining Pt, the lead structure was changed to Al(4)/Pt(2)/Cu(15)/Pt(2) (thickness in nm). Aluminum was used for two reasons: First it alloys fairly aggressively with Pt. Second, it can substitute gallium in the GGG structure. The hope was that these properties would allow the Al layer to absorb any Pt on the surface and try then to bond to the GGG layer. The Pt layer adjacent to the Al layer was an attempt to stabilize the Al layer and prevent migration of Al into the Pt nanowire. The worry was that Al impurities in the Pt layer could cause problems with the spin Hall angle. However, recently it has been presented that Al impurities in Pt actually can increase the spin hall angle [40].

After depositing the leads, the samples are soaked in acetone heated to 60 C for 45 minutes. This serves to dissolve the resist and in theory, only the regions that had been exposed will have material when the procedure is done. The adhesion of leads to GGG is generally poor, so lift off needs to be done carefully. To complete the leads the beaker containing the sample and acetone needs to be gently swirled. When it looks like the material has been lifted off, the sample can be removed from the acetone. It needs to be sprayed wit isopropyl alcohol immediately after removal from acetone or else residue will be left on the sample. Then before it dries, dry nitrogen should be used to remove any liquid.

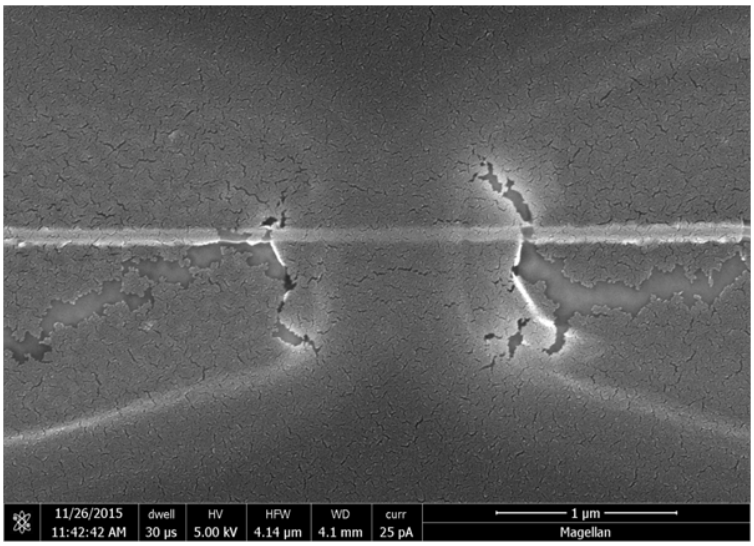

Figure 3.12: SEM image of the lead pattern after development showing a case where the Pt layer on top of the PMMA layer does not break apart.

3.6 Completed Nanowire

After the leads are defined we are left with a completed device. Figure 3.13 shows two examples of completed devices. From the SEM images one would assume that the left wire would have better characteristics than the right one due to the large amount of leftover residue on the wire and slightly torn lead. Surprisingly, the left wire has an almost unintelligible behavior as seen by the ferromagnetic resonance measurement above it. The details of this type of measurement will be explained in the next section, but generally the presence of multiple peaks is bad for spin torque oscillators. In contrast, the wire on the right has a relatively simple spectra and is the fully functioning spin torque oscillator that will be analyzed in the later chapter.

The large difference in behavior is likely due to the design of the nanowires. The left wire in Figure 3.13 was an early version that had a small amount of overlap between the leads and nanowire. This design lead to various problems. The first is the contact resistance from the leads to wire is high. Second, the spin wave spectra for this design is a mess. This likely is due to the spin waves reflecting at the edges of the wire and returning back to the

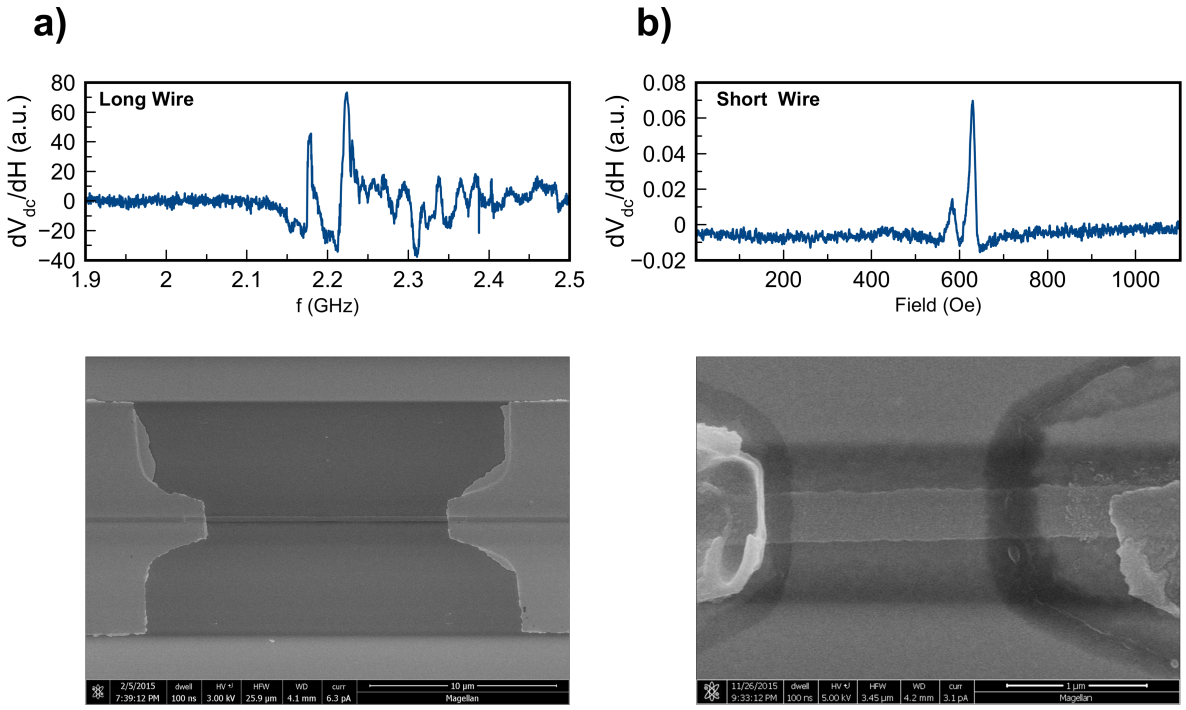

Figure 3.13: **a)** Nanowire with a bad spectra and image of the wire. **b)** Nanowire with a good spectra and image of the wire.

active region. The simple fix for both these issues is to increase the length of the wire under the leads and decrease the active region. The added overlap helps to decrease the contact resistance and any spin waves leaving the active region decay before hitting a reflection point at the edge of the wire. Also the smaller active region decreases the overall sample resistance and improves the impedance mismatch to the microwave circuitry impedance of 50 ohms.

3.7 Alternate Procedure: "Quick and Dirty"

The procedure for STO fabrication described previously in this chapter is the proper way to make samples. Mainly the nonmagnetic leads not only serve to lower the sample resistance, it eliminates any signal from magnetic leads and allows for a simpler boundary condition between the main active region and the rest of the wire. However, this procedure can take

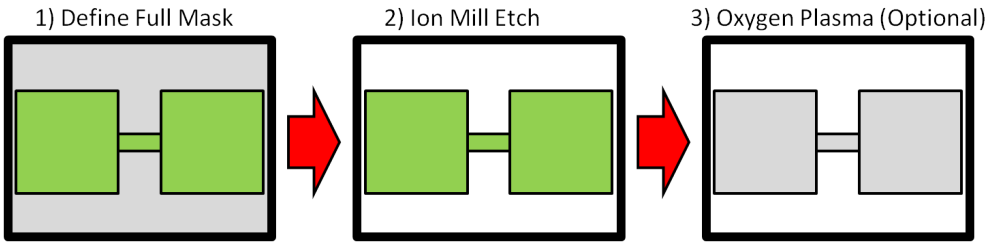

Figure 3.14: Alternate process flow for the fabrication of nanowires used in this study.

a lot of time to complete and can be prone to failure. Sometimes the thin films used are in short supply, so failure is not an option. Other times quick turn around is needed for developing multilayer stacks.

Figure 3.14 shows the general flow for this quicker procedure. In this method, the alignment marks are skipped since they are not needed. First, MAN-2401 resist is spun over the entire sample like in the full procedure. Rather than just writing the wire, the leads are written as well. After development the sample is then etched down to the substrate giving a complete device that can be used. The last step in the procedure is optional, and involves removal of any resist with oxygen plasma etching. If optical access to the sample is not needed, then this step is often skipped.

While this procedure is great for a quick turnaround, there are some other issues with it as well. Figure 3.15 shows a SEM image of a completed device. The pattern used is similar to that in Figure 3.14 but the actual device has a taper to it. This is a common issue with e-beam lithography, where the sections can bleed together. To avoid this the pattern must be drawn in a way where this is taken into account. However, this requires extensive testing and was not done for this sample.

So far most of the fab has been directed towards nanodevices built from films of GGG/YIG/Pt, but nanodevices made from GGG/Pt/YIG were studied as well. These reverse stack samples where prepared on substrates that were smaller than what was desirable. Typically for chips smaller than 10 mm by 10 mm the resists tend to not spin well. With any size chip,

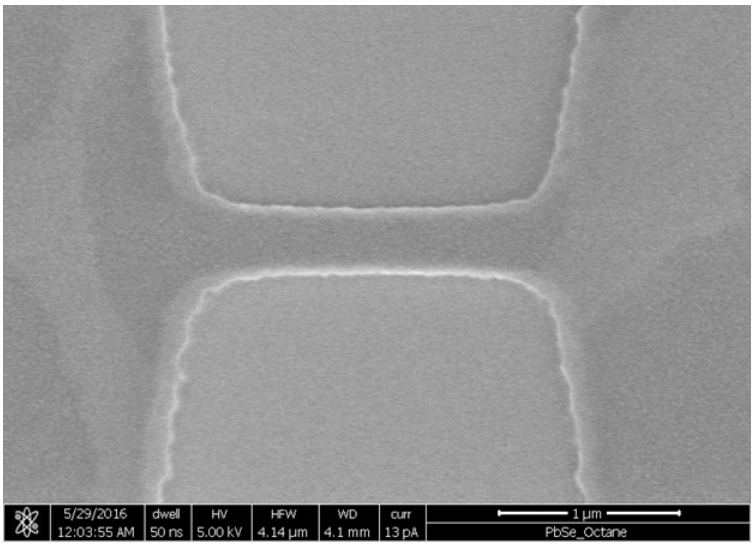

Figure 3.15: SEM image of the lead pattern after development showing a case where the Pt layer on top of the PMMA layer does not break apart.

the resist beads up slightly at the edges. On small chips this causes the resist to be much thicker and the thickness is not uniform across the chip, leading to difficulties in fabrication. Whenever more issues like this are introduced, the probability of a full fabrication procedure failing increases quite a bit. This is where the single step method is desirable. If the first lithography step doesn't work right, acetone can be used to remove the MAN-2401 mask, allowing for a redo.

While the devices made from GGG/Pt/YIG films will not be discussed in detail here, Figure 3.16 shows the field dispersion measured by spin torque ferromagnetic resonance for a device made with this quick procedure. It shows that there is still a usable signal and not too many modes that arise from interactions between the leads and the active part of the wire where the current density is highest. Further studies [41] also have shown that these types of devices can enter auto-oscillations like the full procedure samples.

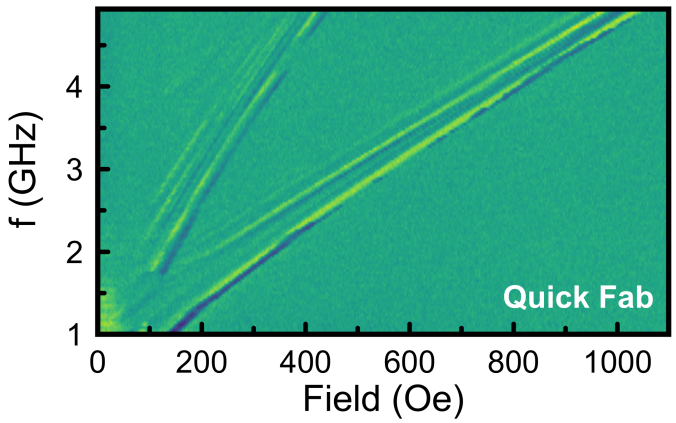

Figure 3.16: Alternate process flow for the fabrication of nanowires used in this study.

Chapter 4

Measurement Techniques and Selected Results

The next section details two specific techniques used in the measurement of the nanowires built in the previous chapter and on magnetic tunnel junctions. Since the end goal is to build a spin torque oscillator, the detection of emitted microwave power is one of the main measurements. However, due to the nature of the materials used, this signal is difficult to measure so a new technique was developed for measuring microwave emission. To narrow down the search region, the devices can be directly driven. These signals are small as well, but are significantly easier to measure and give a good idea of the conditions needed to see a self oscillatory state. The next sections will focus primarily on the techniques used and show only a few representative results.

4.1 Spin Torque Ferromagnetic Resonance (ST-FMR)

In a typical spin torque ferromagnetic resonance experiment, microwave current is directly applied to a sample [10, 42, 43] to excite magnetic oscillations. In the case of the nanowires measured here, the microwave current exerts an ac spin torque and Oersted field drive on the adjacent YIG layer. A DC signal is then produced from the rectification of the microwave drive current and the resistance oscillations during resonance. In the case of a YIG/Pt wire, the resistance oscillations come from a combination of the spin Hall magnetoresistance and inverse spin Hall effect [44].

The general schematic for the equipment and connections needed to perform this type of measurement are shown in Figure 4.1a. A microwave generator is connected to the nanowire through a bias tee which serves to isolate the DC and microwave electronics. The application of DC to the microwave ports on many types of equipment will cause damage so this is critical. On the DC port of the bias tee, the rectified voltage is measured and an additional DC current can be added to study the effect of static spin current.

Since the signal voltage is small relative to the typical noise in this type of circuit, a field modulation technique and lock-in detection is employed [45]. This method is highly sensitive to low level magnetic signals since the modulation scheme only affects voltages that can respond to magnetic fields near where the the modulation field is applied. This differs from the commonly used amplitude modulation technique where the signal produced can still have large background voltages due resonances in the entire circuit.

Most of the measurements presented in this study where performed in the field domain, where the frequency is held constant and the applied field is swept. This provides some advantages for the types of devices measured over those performed in the frequency domain. Mostly this is due to the presence of standing waves in the measurement circuit being enhanced from the sample impedance mismatch from 50 ohms. The standing wave background affects the

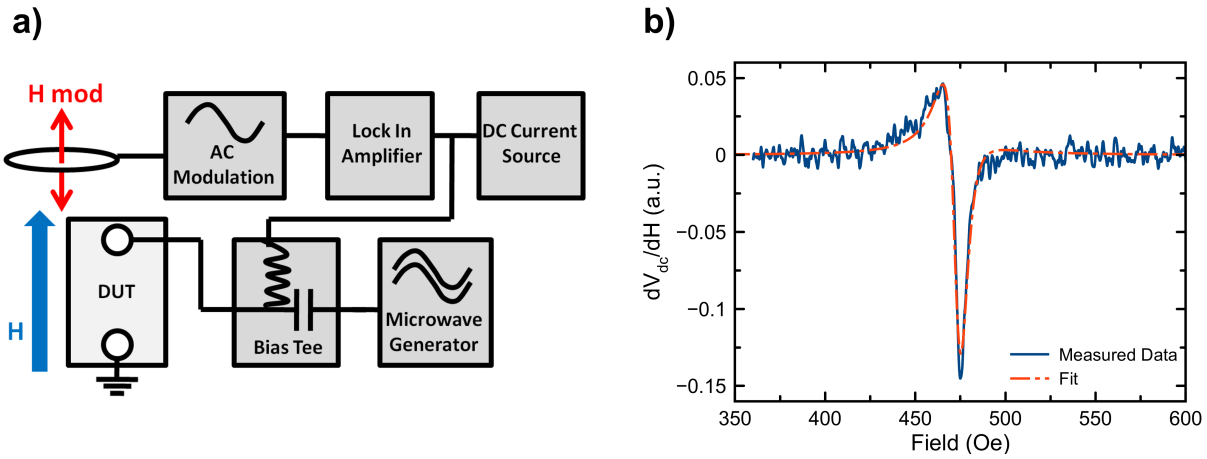

Figure 4.1: **a)** Block diagram for measuring ST-FMR **b)** Example of a measured ST-FMR trace.

power delivered to the sample and impedes measurement. Mainly the measured linewidth will then oscillate slightly. Since YIG is a very low damping material, accurately measuring the linewidth requires all conditions to be constant through the measurement. By switching to field domain, the power delivered for a single trace can be held constant making studies on the DC bias dependence more accurate.

Figure 4.1b shows a single trace created in the field domain using this technique. In conventional FMR, the signal measured is the sum of lorentzian and anti-lorentzian curves. However, the addition of field modulation creates a signal that is the field derivative $\left(dV_{\mathrm{dc}}\left(H\right)/dH\right)$ of a lorentzian and anti-lorentzian. Qualitatively this can be understood as follows, the AC field modulation causes the resonance for a mode to oscillate. Then while sitting at a static applied field the at the edge of a resonance location, the sample will move in and out of resonance producing an AC signal who's amplitude is proportional to the slope of the mode.

By performing this measurement over a range of applied fields and frequencies, the field dispersion relation for a magnetic material or device can be obtained. The field dispersion is governed not only by the magnetic materials of the device, but the shape of it as well [46]. As such the field dispersion provides a powerful diagnostic tool when it comes to spintronics.

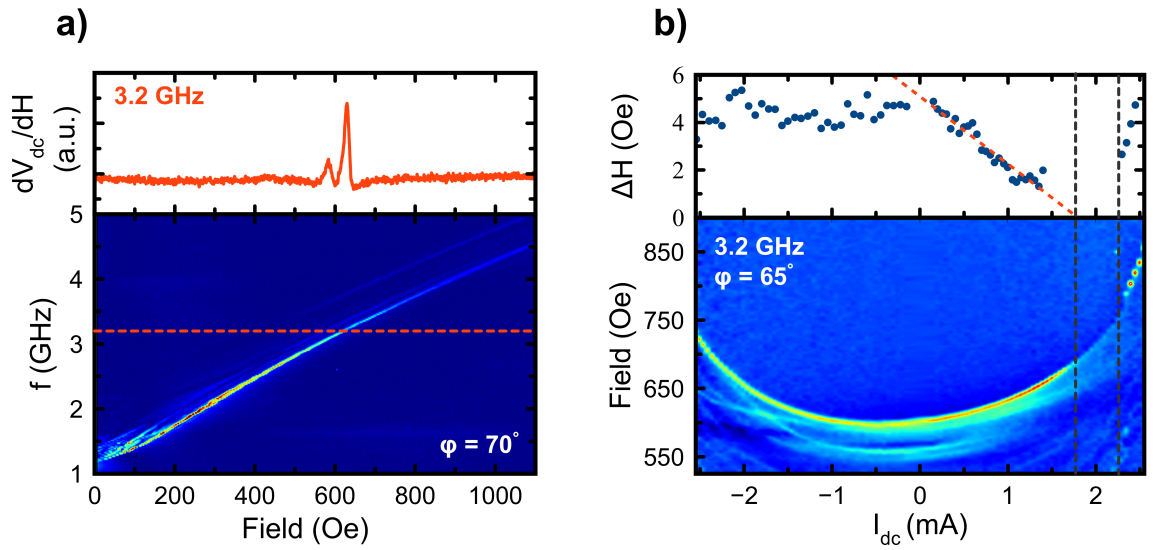

Figure 4.2: **a)** ST-FMR field dispersion with example trace (red dotted line). **b)** Bias dependence taken at 3.2 GHz with linewidth fit above.

Figure 4.2a shows a field dispersion taken for a YIG/Pt nanowire. There are two main branches of modes which are typical for this geometry due to the effective field at the edges of a nanowire being less than the bulk [47]. This leads to two main types of oscillatory modes, one localized at the edges of the wire and another at the center[48]. These two modes then create the branches seen.

By applying DC bias to the same nanowire, the effect of DC spin current injection can be investigated. Figure 4.2b shows a color plot where this is done. The first feature to note is the parabolic nature of the resonance position as a function of applied DC bias. This arises from the heating in the wire decreasing the saturation magnetization [9, 28]. The asymmetry in the position (linear component) is related to the Oersted field from the applied current. The next feature of interest occurs if we follow the bias dependence main edge mode as identified from micromagnetic simulations. For positive currents, we see a region as indicated by the dotted lines in Figure 4.2b where the line seems to disappear. After this region it returns with a larger amplitude and a shift in resonance position from the parabolic dependence. Although the exact reason for this disappearance is not clear, the behavior of the mode's linewidth near this region, as shown at the top of Figure 4.2b, provides some clues to what

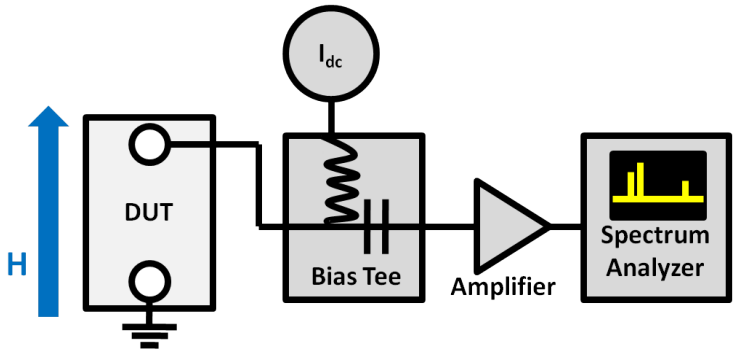

Figure 4.3: Block diagram for a direct measurement of microwave emission from a spin torque oscillator.

it happening. From zero bias we see a decrease in linewidth. If we follow this trend to zero linewidth, it corresponds to the region where the mode disappears in the color plot. Then in the region it reappears the linewidth is being broadened. Combining the linewidth behavior with the shift in resonance position, this provides the first indication of how much bias is required to reach the self oscillatory state.

4.2 Field Modulated Spectrum Analyzer

Spectrum analyzers are a powerful tool for measuring microwave power at multiple frequencies since conceptually, they act like performing a fast Fourier transform on any incoming signal. This function makes one invaluable for the measurement of microwave emission from a spin torque oscillator. Traditionally for this measurement, the equipment is configured in a manner similar to Figure 4.3. The sample is supplied DC current through the DC port of a bias tee and the emission is then detected on the RF port of the bias tee. Usually a low noise microwave amplifier is placed before the spectrum analyzer to increase the signal quality. For many types of samples this method has been successful since their output power is well within the detectable range of a typical analyzer-amplifier combo. However, in the case of a YIG/Pt based oscillator the output power is too low to measure by this method.

In principle one would think that increasing the amount of points averaged would allow for a low level signal to be measured. This comes with a cost in time that not only makes the measurement time prohibitive, but can make the measurement inaccurate. Typically in the cryostat there is a slight temperature drift over long periods of time which will shift the center frequency of the emitted power slightly over time. If the measurement period is long, the measured peak will then be artificially broadened. To improve the measurement quality and speed, moving to a modulated technique is desirable since the lock-in measurement technique is powerful for picking out low level signals in a noisy environment. This is implemented in a manner similar to the previous section with the introduction of field modulation.

The field modulated spectrum analyzer method is as follows in the block diagram in Figure 4.4a. Like the direct method, DC current is supplied to the sample through a bias tee. The main difference is the configuration of the spectrum analyzer. Normally measurements are made in the frequency domain on a spectrum analyzer, but there is a mode called "zero span" where the detection frequency can be fixed and then the power over time is displayed. In this mode the analyzer essentially acts as a bandpass filter for a selected frequency and allows for the field modulation technique to be employed. If an emission peak is at the edge of the detected frequency, the field modulation will shift the resonance frequency such that it moves in and out of the bandpass filter, creating an AC signal. This AC signal can be passed to a lock-in amplifier through the video output on the analyzer.

Since the power emitted from a YIG based oscillator is small [14, 15] due to having a small MR ratio, it is best to first benchmark this new technique using a different type of sample. A magnetic tunnel junction is a good system to test this method since it has high magnetoresistance. The field dispersion and its bias dependence is easily measurable with the ST-FMR method described earlier allowing for quick determination of the conditions needed to reach a self oscillatory state. Further, the self oscillatory state does not need to be reached to observe microwave power from this type of device. The high MR allows for

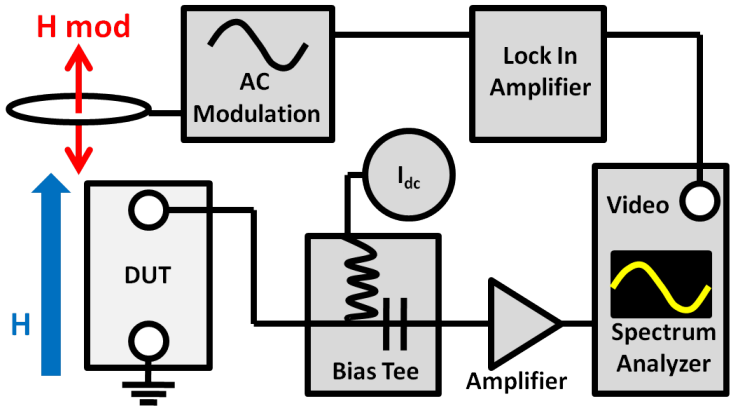

Figure 4.4: Block diagram for the field modulated spectrum analyzer measurement technique.

easier observation of thermal FMR, where even small thermal fluctuations in magnetization will give way to a measurable microwave power.

The signal produced by field modulation technique can be seen in Figure 4.5a along with the direct method. In general, the emission peaks should be lorentzian shaped in the normal measurement method. Like the field modulated ST-FMR described earlier, the signal measured with modulation is the field derivative $(dP(H)/dH)$ of the emission signal. Since the lock-in integration time is a form of averaging, to compare the effectiveness of field modulation the traces are acquired such that they have the same data density and require the same time to complete. Clearly the signal to noise ratio for the field modulated trace is improved over the direct measurement.

To further illustrate the improvement made by this new technique, color plots for the detected microwave as a function of bias and frequency are made and are shown in Figure 4.5bc. As with the single traces, the averaging on the plots is such that they require the same amount of time to generate. Again a large increase in signal to noise is seen with the addition of field modulation. In both approaches the lowest frequency mode is seen at high bias, but field modulation allows for it to be observed at much lower biases. On top of this field modulation reveals another high frequency mode that is not visible in the plot generated with conventional means.

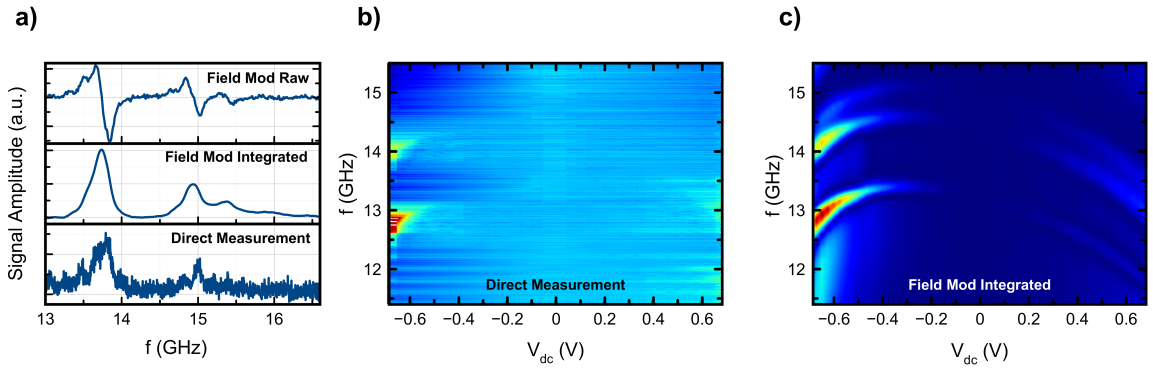

Figure 4.5: **a)** Comparison of single traces for the direct spectrum analyzer method and field modulated method. **b)** Color plot of the emission power as a function of bias voltage using the direct method and **c)** using field modulation.

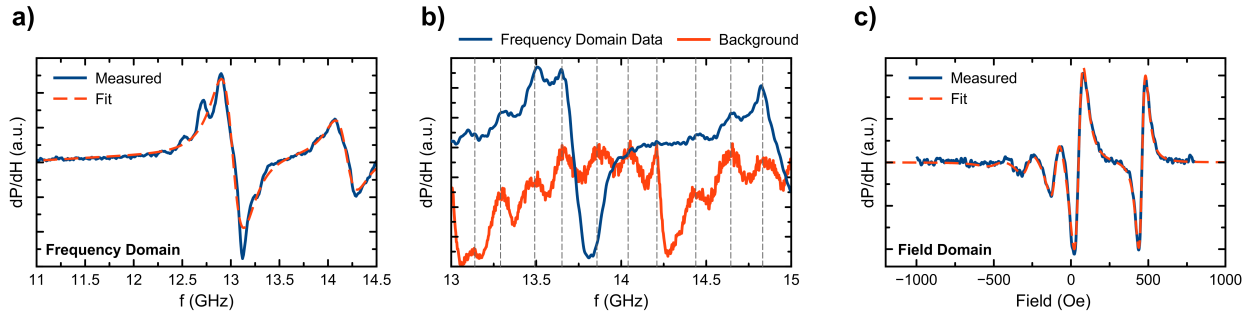

Figure 4.6: **a** Single field modulated spectrum analyzer with lorentzian derivative fit. **b** Demonstration on the standing wave background's effect on the trace taken in the frequency domain. **c** Single trace taken in the field domain showing the suppression of artifacts from the standing wave background

With the field modulation technique there is the choice of measuring in either the field or frequency domains. In typical emission experiments the frequency domain has been chosen since the spectrum analyzer trace acquisition is meant to work this way when used in the spectrum analyzer mode. However, in the frequency domain there exist oscillations in the background due to the presence of standing waves. When measuring in the frequency domain these still impact the measurement as seen in the oscillations from the fit in Figure 4.6a. These oscillations are directly related to the background as shown in Figure 4.6b where the direct measurement of the background is compared to a trace. The dotted lines indicate maxima for the background and they appear in the field modulated trace as well.

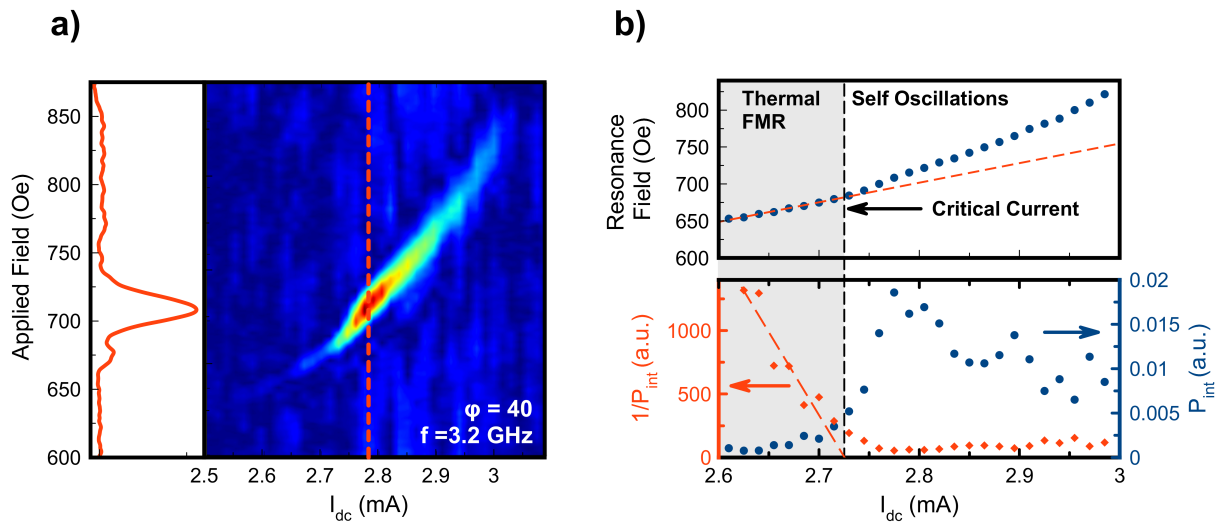

Figure 4.7: **a)** Color plot showing the emission of microwave power from a YIG/Pt spin torque oscillator. **b)** Fits of the data represented in the color plot to the right.

In principle the field modulation technique should ignore any background which makes the observation of these oscillations surprising. Their presence may be directly related to the physics of microwave circuits rather than just poor background subtraction. It has been recently shown that a spin torque oscillator's performance can be altered by locking to itself [49]. This was accomplished by placing a delay line before the spectrum analyzer to change the phase of the power that gets reflected back to the spin torque oscillator. Since the standing waves in the circuit are due to similar interference of reflected waves, it is possible that in the frequency domain these oscillations are inevitable without controlling the phase of reflected power.

A simple approach to decrease the contribution from the standing waves is to perform the measurements in the field domain where the frequency is held constant. The reflected power will still alter the spin torque oscillator properties, but it will be a constant offset throughout the measurement, rather than an oscillating perturbation. Figure 4.6c shows a trace taken in this domain and compared to the frequency domain, we see an almost perfect fit to the theoretical model for an emission peak.

This new measurement technique allowed for the direct measurement on a YIG/Pt based spin torque oscillator. Unlike the MTJ described earlier, the MR is low at about roughly .01 percent. This is five orders of magnitude lower than a typical MTJ. The power from a device like this will lie in the femptowatt level and on top of low power, impedance mismatches will decrease the fraction of this power that can be detected.

In Figure 4.7a, the color plot shows the detection of microwave emission power from a YIG/Pt nanowire, with a single trace shown on the side. Fitting the individual traces gives the data seen in Figure 4.7b. As the bias applied to the nanowire is increased, we see an increase in the detected microwave power around 2.7 mA. The critical current can be estimated from looking at the inverse of the integrated power and extracting it to zero [50]. This point where it reaches near zero we observe a shift in the resonance field. This shift is related to the average magnetization decreasing when the going into auto-oscillations.

Chapter 5

Conclusion

In conclusion the fabrication of a YIG/Pt based spin torque oscillator was achieved. In the process of reaching this goal several types of preliminary work needed to be completed. A complete measurement station was assembled and several tools designed to increase the possible signal where developed. Once the groundwork was laid, samples where made using e-beam lithography and ion milling techniques. These samples where then measured using ST-FMR and indicated that they where potential spin torque oscillators. However detection of microwave power proved to be difficult so a new method needed to be developed and tested. Once this was done the detection of microwave emission from YIG/Pt was possible

Future work will detail the unique properties of these devices. Since YIG is an insulating material, it opens up the observation of different sources of pure spin currents. Specifically the heating in these devices leads to the generation of spin currents that add to the spin Hall effect and reduce the current required to reach the oscillatory state.

Bibliography

[1] Slonczewski, J. Current-driven excitation of magnetic multilayers. *J. Magn. Magn. Mater.* **159**, L1–L7 (1996).

[2] Sun, J. Z. Current-driven magnetic switching in manganite trilayer junctions. *J. Magn. Magn. Mater.* **202**, 157–162 (1999).

[3] Miron, I. M. *et al.* Perpendicular switching of a single ferromagnetic layer induced by in-plane current injection. *Nature* **476**, 189–193 (2011).

[4] Worledge, D. C. *et al.* Spin torque switching of perpendicular Ta—CoFeB—MgO-based magnetic tunnel junctions. *Appl. Phys. Lett.* **98**, 98–101 (2011).

[5] Liu, L. *et al.* Spin-Torque Switching with the Giant Spin Hall Effect of Tantalum. *Science (80-.).* **336**, 555–558 (2012).

[6] Landau, L. & Lifshits, E. on the Theory of the Dispersion of Magnetic Permeability in Ferromagnetic Bodies. *Phys. Zeitsch. der Sow.* **169**, 14–22 (1935).

[7] Gilbert, T. A lagrangian formulation of the gyromagnetic equation of the magnetization field. *Phys. Rev.* **100**, 1243 (1955).

[8] Kiselev, S. I. *et al.* Microwave oscillations of a nanomagnet driven by a spin-polarized current. *Nature* **425**, 380–383 (2003).

[9] Petit, S. *et al.* Spin-torque influence on the high-frequency magnetization fluctuations in magnetic tunnel junctions. *Phys. Rev. Lett.* **98**, 3–6 (2007).

[10] Liu, L., Moriyama, T., Ralph, D. C. & Buhrman, R. A. Spin-torque ferromagnetic resonance induced by the spin Hall effect. *Phys. Rev. Lett.* **106**, 1–4 (2011).

[11] Demidov, V. E. *et al.* Magnetic nano-oscillator driven by pure spin current. *Nat. Mater.* **11**, 1028–1031 (2012).

[12] Liu, L., Pai, C. F., Ralph, D. C. & Buhrman, R. A. Magnetic oscillations driven by the spin hall effect in 3-terminal magnetic tunnel junction devices. *Phys. Rev. Lett.* **109**, 1–5 (2012).

[13] Duan, Z. *et al.* Nanowire spin torque oscillator driven by spin orbit torques. *Nat. Commun.* **5**, 5616 (2014).

[14] Collet, M. *et al.* Generation of coherent spin-wave modes in yttrium iron garnet microdiscs by spin-orbit torque. *Nat. Commun.* **7**, 10377 (2016).

[15] Safranski, C. *et al.* Spin caloritronic nano-oscillator. *Nat. Commun.* **8**, 117 (2017).

[16] Thirion, C., Wernsdorfer, W. & Mailly, D. Switching of magnetization by nonlinear resonance studied in single nanoparticles. *Nat. Mater.* **2**, 524–527 (2003).

[17] Rivkin, K. *et al.* Physical principles of microwave assisted magnetic recording **214312** (2017).

[18] Thomson, W. On the Electro-Dynamic Qualities of Metals:–Effects of Magnetization on the Electric Conductivity of Nickel and of Iron. *Proc. R. Soc. London* **8**, 546–550 (1856).

[19] Nakayama, H. *et al.* Spin Hall Magnetoresistance Induced by a Nonequilibrium Proximity Effect. *Phys. Rev. Lett.* **110**, 1–5 (2013).

[20] Avci, C. O. *et al.* Unidirectional spin Hall magnetoresistance in ferromagnet/normal metal bilayers. *Nat. Phys.* **11**, 570–575 (2015).

[21] Baibich, M. N. *et al.* Giant magnetoresistance of (001)Fe/(001)Cr magnetic superlattices. *Phys. Rev. Lett.* **61**, 2472–2475 (1988).

[22] Binasch, G., Grünberg, P., Saurenbach, F. & Zinn, W. Enhanced magnetoresistance in layered magnetic structures with antiferromagnetic interlayer exchange. *Phys. Rev. B* **39**, 4828–4830 (1989).

[23] Miyazaki, T. & Tezuka, N. Giant magnetic tunneling effect in Fe/Al2O3/Fe junction. *J. Magn. Magn. Mater.* **139**, 94–97 (1995).

[24] Moodera, J. S., Kinder, L. R., Wong, T. M. & Meservey, R. Large magnetoresistance at room temperature in ferromagnetic thin film tunnel junctions. *Phys. Rev. Lett.* **74**, 3273–3276 (1995).

[25] Tsoi, M. *et al.* Excitation of a magnetic multilayer by an electric current. *Phys. Rev. Lett.* **80**, 4281–4284 (1998).

[26] Butler, W. H., Zhang, X.-G., Schulthess, T. C. & MacLaren, J. M. Spin-dependent tunneling conductance of Fe—MgO—Fe sandwiches. *Phys. Rev. B* **63**, 054416 (2001).

[27] Dyakonov, M. I. & Perel, V. I. Possibility of orientating electron spins with current. *Sov. Phys. JETP Lett.* **13**, 467 (1971).

[28] Hamadeh, A. *et al.* Full control of the spin-wave damping in a magnetic insulator using spin-orbit torque. *Phys. Rev. Lett.* **113**, 1–5 (2014).

[29] Uchida, K. I. *et al.* Observation of longitudinal spin-Seebeck effect in magnetic insulators. *Appl. Phys. Lett.* **97** (2010).

[30] Xiao, J., Bauer, G. E. W., Uchida, K.-c., Saitoh, E. & Maekawa, S. Theory of magnon-driven spin Seebeck effect. *Phys. Rev. B* **81**, 214418 (2010).

[31] Hoffman, S., Sato, K. & Tserkovnyak, Y. Landau-Lifshitz theory of the longitudinal spin Seebeck effect. *Phys. Rev. B - Condens. Matter Mater. Phys.* **88**, 1–8 (2013).

[32] Rezende, S. M. *et al.* Magnon spin-current theory for the longitudinal spin-Seebeck effect. *Phys. Rev. B - Condens. Matter Mater. Phys.* **89**, 1–10 (2014).

[33] Lu, L., Sun, Y., Jantz, M. & Wu, M. Control of ferromagnetic relaxation in magnetic thin films through thermally induced interfacial spin transfer. *Phys. Rev. Lett.* **108**, 1–5 (2012).

[34] Jungfleisch, M. B. *et al.* Heat-induced damping modification in yttrium iron garnet/platinum hetero-structures. *Appl. Phys. Lett.* **102** (2013).

[35] Lauer, V. *et al.* Auto-oscillations in YIG/Pt microstructures driven by the spin Seebeck effect arXiv:1612.07305 (2016).

[36] Rosas, B. Optimizing Test Boards for 50 GHz End Launch Connectors .

[37] Chang, H. *et al.* Nanometer-Thick Yttrium Iron Garnet Films With Extremely Low Damping. *IEEE Magn. Lett.* **5**, 6700 (2014).

[38] Barsukov, I. *et al.* Magnetic phase transitions in Ta/CoFeB/MgO multilayers. *Appl. Phys. Lett.* **106** (2015).

[39] Yang, H. *et al.* Electron beam lithography of HSQ/PMMA bilayer resists for negative tone lift-off process. *Microelectron. Eng.* **85**, 814–817 (2008).

[40] Ngyuyen, M. H., Zhao, M., Ralph, D. C. & Buhrman, R. A. APS March Meeting 2016, http://meetings.aps.org/link/BAPS.2016.MAR.K18.8 .

[41] Evelt, M. *et al.* Spin Hall-induced auto-oscillations in ultrathin YIG grown on Pt. *Sci. Rep.* **8**, 1269 (2018).

[42] Tulapurkar, A. A. *et al.* Spin-torque diode effect in magnetic tunnel junctions. *Nature* **438**, 339–342 (2005).

[43] Sankey, J. C. *et al.* Spin-transfer-driven ferromagnetic resonance of individual nanomagnets. *Phys. Rev. Lett.* **96**, 50–53 (2006).

[44] Chiba, T., Bauer, G. E. & Takahashi, S. Current-Induced Spin-Torque Resonance of Magnetic Insulators. *Phys. Rev. Appl.* **2**, 034003 (2014).

[45] Gonçalves, A. M. *et al.* Spin torque ferromagnetic resonance with magnetic field modulation. *Appl. Phys. Lett.* **103** (2013).

[46] Kittel, C. On the theory of ferromagnetic resonance absorption. *Phys. Rev.* **73**, 155–161 (1948).

[47] Bayer, C. *et al.* Spin-wave excitations in finite rectangular elements of Ni80Fe20. *Phys. Rev. B* **72**, 064427 (2005).

[48] Duan, Z. *et al.* Spin wave eigenmodes in transversely magnetized thin film ferromagnetic wires. *Phys. Rev. B - Condens. Matter Mater. Phys.* **92**, 1–10 (2015).

[49] Tsunegi, S. *et al.* Self-Injection Locking of a Vortex Spin Torque Oscillator by Delayed Feedback. *Sci. Rep.* **6**, 1–7 (2016).

[50] Slavin, A. & Tiberkevich, V. Advances in Magnetics Nonlinear Auto-Oscillator Theory of Microwave Generation by Spin-Polarized Current **45**, 1875–1918 (2009).

Appendix A

Resist Recipes

This section details the recipes for spinning and developing the types of resists used in this study.

A.1 MAN-2401

MAN-2401 is a useful negative resist that can be removed making it good for a hard mask. It is UV sensitive so best to avoid exposure. The recipe to use is as follows:

- **Clean:** Ensure the surface of the chip is clean. If not sonicate in acetone then isopropyl alcohol.
- **Spin Coating:** Spin at 3500 rpm for 45 seconds.
- **Bake:** Bake the sample on a hotplate for 60 seconds at 90 degrees C.
- **EBL Writing:** The general dosage for this resist ranges from 250 - 300 in the NPGS software.

- **Development:** The devolper for this is maD-525 and is used for 60 seconds. Then rinse with HPLC water for 3 minutes. Sometimes extra development is needed and this is done in an as needed manner.
- **Removal:** Sometimes can be removed with acetone but usually needed oxygen plasma cleaning to be removed. If it does not need to be removed for another fab step, the wirebonder can easily make contact through the resist.

A.2 PMMA

PMMA is a versatile positive resist that is commonly used for EBL.

- **Clean:** Ensure the surface of the chip is clean. If not sonicate in acetone then isopropyl alcohol.
- **Prebake:** Prebake the sample on the hotplate for 1.5 minutes at 180 degrees C.
- **Spin Coating:** Spin at 3500 rpm for 45 seconds.
- **Bake:** Bake the sample on a hotplate for 1.5 minutes at 180 degrees C.
- **EBL Writing:** The general dosage for this resist is around 300 in the NPGS software.
- **Development:** The devolper for this is a 1:3 volume mix of methyl isobutal keytone and isopropyl alcohol. Development time is roughly 45 seconds. Clean the sample immediately after development with isopropyl alcohol.
- **Removal:** Usually acetone works well. Soak for at least 30 minutes.

A.3 MMA

PMMA is a versatile positive resist that is commonly used for EBL.

- **Clean:** Ensure the surface of the chip is clean. If not sonicate in acetone then isopropyl alcohol.
- **Prebake:** Prebake the sample on the hotplate for 1.5 minutes at 180 degrees C.
- **Spin Coating:** Spin at 3500 rpm for 45 seconds.
- **Bake:** Bake the sample on a hotplate for 1.5 minutes at 180 degrees C.
- **EBL Writing:** The general dosage for this resist is around 300 in the NPGS software.
- **Development:** The devolper for this is a 1:3 volume mix of methyl isobutal keytone and isopropyl alcohol. Development time is roughly 45 seconds. Clean the sample immediately after development with isopropyl alcohol.
- **Removal:** Usually acetone works well. Soak for at least 30 minutes.

Appendix B

YIG/Pt Nanowire Fabrication Process

Film Preparation:

- Deposit Yttrium Iron Garnet on Gadolinium Gallium Garnet [37]
- Load into UCI sputtering chamber
- Argon clean surface
- Deposit Platinum at room temperature

Alignment Marks:

- Spin coat MMA followed by PMMA
- Using e-beam lithography, write array of alignment marks. Typically a write current of 3.2 nA is used with an area dose of 270
- Develop for 45 seconds
- Sputter 30 nm of Tantalum

- Soak in acetone heated to 60 C for 45 minutes
- Sonicate briefly

Nanowire Definition:

- Spin coat MAN-2401
- Using e-beam lithography, align nanowire to previously made alignment marks. Typical write current is 13 pA and area dose of 270. Center to center distance and line spacing set to 1 nm
- Develop for 60 seconds
- Etch in ion mill. In our system Pt etches at 9 nm/min and YIG at 3.7 nm/min. Etch angle is typically 65 degrees with a 25% duty cycle.
- Oxygen plasma etch in Harrick O2 cleaner for 9 minutes at high power.

Lead Deposition:

- Spin coat MMA followed by PMMA
- Sputter coat 2 nm of Platinum
- Using e-beam lithography, align to previously made alignment marks. Typical write current for section closest to the wire is 13 pA and area dose of 270. Center to center distance and line spacing set to 1 nm. Then for larger features the current is increased in steps to up to 3.2 nA.
- Develop for a minute shaking aggressively
- Sputter deposit lead material: Al(4)/Pt(2)/Cu(15)/Pt(2)

- Soak in acetone heated to 60 C for 45 minutes
- Swirl gently and use spray bottle of acetone for lift off